

Non-local resources for error correction in quantum LDPC codes

Omprakash Chandra,* Gopikrishnan Muraleedharan, and Gavin K. Brennen

*Center for Engineered Quantum Systems, School of Mathematical
and Physical Sciences, Macquarie University, 2109 NSW, Australia*

(Dated: September 10, 2024)

Scaling fault-tolerant quantum computing is essential to realize the potential of quantum computation. Surface code has been the best choice over the last decade because of its effective error suppression capability. However, it suffers from a low encoding rate, requiring a vast number of physical qubits for large-scale quantum computation. In contrast, hypergraph product codes present a promising alternative, as both their encoding rate and distance scale with block size. Despite this, their non-local stabilizers necessitate long-range connectivity for stabilizer measurements, posing significant experimental challenges. Recent advancements have shown how to deterministically perform high-fidelity cavity enabled non-local many-body gates, enabling the creation of non-local cat states. We integrate the non-local resource into the DiVincenzo-Aliferis method for fault-tolerant stabilizer measurement. We apply the scheme to long-range quantum hypergraph product codes, performing circuit-level noise simulations including the the cavity error model, achieving a promising threshold. Additionally, we propose a tri-layer architectural layout for scheduling stabilizer measurements, enhancing circuit parallelizability.

I. INTRODUCTION

Quantum computing holds promises for solving problems that are intractable for classical computers, with applications ranging from cryptography and optimization to materials science and drug discovery [1–4]. However, the physical realization of quantum computing is fraught with challenges, primarily due to the fragility of quantum information. Qubits are extremely susceptible to errors arising from environmental noise, imperfect control operations. These errors can rapidly degrade the information stored in a quantum computer, rendering computations unreliable. Thus, quantum error correction (QEC) is essential for building practical and scalable quantum computers [5]. Without QEC, the error rates in current quantum systems would accumulate too quickly, making meaningful quantum computation impossible.

Quantum error correction involves encoding logical qubits into a larger number of physical qubits in such a way that errors can be detected and corrected [6]. Various QEC codes have been proposed, with the surface code being one of the most well-known and extensively studied [7–9]. The surface code has several advantages: it has high threshold for error rates, relatively straightforward decoding, and geometrically local stabilizer measurements which makes it compatible with nearest neighbour connected two-dimensional architectures [10]. These features make it a popular choice for current experimental implementations of fault-tolerant quantum computers [11–13]. Despite its advantages, the surface code has significant limitations hindering scalability, primarily due to a poor encoding rate. Asymptotically, the encoding rate, defined as the ratio of the number of logical qubits k to the number of physical qubits n , approaches zero as $n \rightarrow \infty$ [14]. In fact, this is an

issue for all topological codes in two dimensions with short range interactions. According to the Bravyi-Poulin-Terhal (BPT) theorem [14], for in two dimensions with local commuting constraints $kd^2 \leq cn$, where d denotes distance of a code and c is a constant that solely depends on the locality of the projectors or stabilizers defining the code space and dimension of the Hilbert space describing individual particles. This means we cannot have both a high-distance and a high-encoding rate in a code at the same time.

Hypergraph product codes (HGP) [15] are a type of quantum low density parity check codes (qLDPC) that offer a promising alternative to surface codes. Both their encoding rate and distance scales favourably with the block size of the code, i.e., $k \propto O(n^\alpha)$ and $d \propto O(n^\beta)$, for some $\alpha, \beta > 0$. Recent work demonstrates that HGP codes exhibit high error correction thresholds [16], which means they can tolerate higher error rates before failing. This robustness makes them particularly well-suited for near-term quantum processors, where error rates are still relatively high. The high thresholds of HGP codes are achieved by utilizing advanced decoding algorithms, such as BPOSD [17] and BPLSD [18], in combination with overlapping window techniques [19], which efficiently manage the complex error patterns in these codes. However, HGP codes encounter difficulties with stabilizer measurement because their stabilizers are non-local. This requires complex operations that current technology finds challenging to implement.

Recent research has demonstrated the potential to implement HGP codes in real quantum systems. For instance, the experimental advancement of neutral atom quantum computing using Rydberg interactions has shown significant promise [20–22]. There have been proposals to shuffle qubits for the implementation of non-local gates [23]. However, shuffling is a complex and time-consuming process that reduces the number of stabilizers that can be measured simultaneously, and also

* omprakash.chandra@hdr.mq.edu.au

introduces errors during the process. There have been proposals of using dipole-dipole interactions between Rydberg states for performing long range gates [24, 25]. However, in the long-range, the strength of the van-der-Waals interaction decreases as $1/r^6$, which strictly limits the achievable non-locality. Additionally, parallelization is restricted for these cases: when performing a coupling gate, another cannot be done within the Rydberg blockade radius [26]. The first issue constrains us from implementing long-range HGP codes, which offer very high encoding rate and fairly high distance. The second issue hampers circuit parallelizability, increasing the overall QEC time and introducing several other errors.

We present a scheme that provides a solution for implementing long-range gates in qLDPC codes, such as HGP codes. Recent advancements have demonstrated high-fidelity non-local many-body gates by coupling qubits to a common bosonic mode, which enables the preparation of non-local GHZ states and more general multi-qubit gates with the qubits in place [27]. This approach avoids the complexity associated with shuffling. As suggested in Ref. [27], we integrate these non-local gates into the DiVincenzo-Aliferis method for fault-tolerant stabilizer measurement [28]. As proof of principle, we analyze first the $[[7, 1, 3]]$ Steane code and show that the scheme is fault-tolerant. The advantage is that we need only two rounds of non-local resources per stabilizer measurement: one non-local gates for encoding ancilla qubits into a GHZ state, and a second for decoding the ancilla qubits. We extend this technique to long-range HGP codes and present numerical results demonstrating high thresholds. We propose a scheduling scheme for measuring stabilizers using a tri-layer architecture to enhance the circuit parallelizability. We also discuss some near term algorithms that are implementable using our scheme.

The rest of the article is organized as follows. In Sec. II, we review essential concepts including non-local many-body gates in Sec. II A, syndrome extraction circuits in Sec. II B, and stabilizer quantum codes in Sec. II C. In Sec. III, we implement the DiVincenzo-Aliferis method of syndrome extraction, utilizing non-local many-body gates on the Steane code. In Sec. IV, the same method is applied to Hypergraph Product (HGP) codes. Section V introduces a tri-layer architecture for efficient syndrome extraction. We discuss the strategic placement of cavities and explore the scheduling and parallelizability of syndrome measurements including analysis of full error correction time. Finally, in Sec. VI, we summarize our study, discussing the challenges and near-term algorithms applicable to Rydberg atom quantum computers, followed by a discussion of future directions.

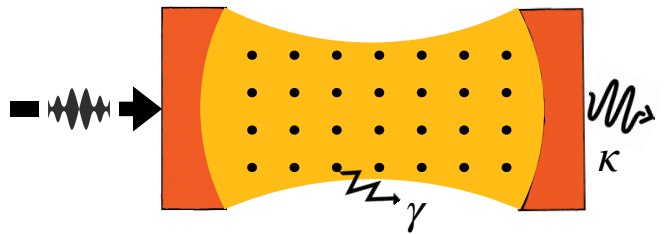


FIG. 1. Illustration of the basic setup for the scheme with a cavity containing an array of three level spins spanned by a qubit and an excited state $|e\rangle$. The cavity mode is driven by an external classical field $\eta(t)$ and decays at rate κ , while $|e\rangle$ leaks at a rate γ to states outside the qubit space.

II. TOOLS

A. Non-local many body gates

We recapitulate the scheme introduced in [27] in order to motivate the form of the non-local gate, its associated error, and the embedding architecture described in Sec. V. The setup consists of N three-level systems with computational basis states $|0\rangle$ and $|1\rangle$, and an excited state $|e\rangle$ with the transition frequencies ω_0 for $|0\rangle \leftrightarrow |1\rangle$ and ω_e for $|1\rangle \leftrightarrow |e\rangle$. A cavity mode, with annihilation (creation) operators $\hat{a}(\hat{a}^\dagger)$ and frequency ω_c , couples the transition $|1\rangle \leftrightarrow |e\rangle$ with coupling strength g . This cavity mode is driven by a complex classical field, $\eta(t)$, according to $H_{\text{drive}} = 2|\eta| \sin(\omega_L t - \arg(\eta))(\hat{a}^\dagger + \hat{a})$.

This classical field is detuned from the cavity by $\delta = \omega_c - \omega_L$ and from the $|1\rangle \leftrightarrow |e\rangle$ transition by $\Delta = \omega_e - \omega_L$. The Hamiltonian is then transformed to the interaction picture (rotating frame) defined by the unitary, $\hat{U}_r(t) = \exp\left[it(\omega_L(\hat{a}^\dagger \hat{a} + \hat{n}_e) + \sum_j \omega_0 |0_j\rangle \langle 0_j|)\right]$. We assume that $|e\rangle$ decays at a rate γ and treat it as leakage outside the qubit subspace by the introduction of a non-Hermitian term to the Hamiltonian. This will provide an expression for fidelity below which is exact in the case of full leakage and is a lower bound otherwise. After applying the rotating wave approximation one arrives at the effective Hamiltonian,

$$\hat{H}_{\text{eff}} = \delta \hat{a}^\dagger \hat{a} + (\Delta - i\gamma/2) \hat{n}_e + [(g\hat{S}^- + i\eta)\hat{a}^\dagger + hc], \quad (1)$$

where, $\hat{n}_e = \sum_j |e_j\rangle \langle e_j|$, $\hat{S}^+ = \sum_j |e_j\rangle \langle 1_j|$, $\hat{S}^- = (\hat{S}^+)^\dagger$. The system evolves under the Lindblad master equation $\dot{\rho} = -i\hat{H}_{\text{eff}}\rho + i\rho\hat{H}_{\text{eff}}^\dagger + L\rho L^\dagger - \{L^\dagger L, \rho\}/2$. Here, $L = \sqrt{\kappa}\hat{a}$ is the jump operator, and $1/\kappa$ is the lifetime of excitation in the cavity mode. We use a time-dependent pulse $\eta(t)$ over a duration T , with $\eta(0) = \eta(T) = 0$, while g , δ , and Δ remain constant throughout the process. As described in Ref. [27], in the large detuning limit, keeping T and η/Δ constant ($T \sim 20 \times g^{-1}$ suffices), there exists a pulse profile that can generate a high-fidelity Mølmer-Sørensen type gate, $U = e^{i\theta \hat{J}_z^2}$, where $\hat{J}_z = \frac{1}{2} \sum_{j=1}^N Z_j$ represents the \hat{z} component of the collective spin.

To make the gate address only a subset of ancillary qubits needed for a cat state, one can adopt a variety of approaches: shelve the $|1\rangle$ state for qubits that should be spectators to an ancillary state $|a\rangle$ that doesn't couple to the cavity, or use addressable large AC-stark shifts applied only on the relevant ancilla to make them interact strongly with the cavity leaving the rest too far detuned to interact, or use a different species of spins for the ancilla with addressable transitions in frequency and space.

The evolution under the Hamiltonian \hat{H}_{eff} , in the absence of any losses ($\gamma, \kappa = 0$), is a unitary transformation given by $\hat{U} = e^{i\theta \hat{J}_z^2}$. In the presence of losses, due to cavity decay and excited state decay of the spins, the evolution is no longer unitary and is described by a map given by,

$$\mathcal{E}_{\text{eff}}(\rho) = \sum_{m,m'} \rho_{m,m'} e^{i\theta_{m,m'}} |m\rangle \langle m'| \quad (2)$$

where,

$$\theta_{m,m'} \approx [(m^2 - m'^2) + (m - m')N] \theta + \frac{(m - m')^2 i \theta}{\sqrt{C} d_N} + \frac{(m + m' + N) i \theta d_N}{2\sqrt{C}}. \quad (3)$$

Here, $C = g^2/\kappa\gamma$ denotes the cooperativity, and $d_N = [2(1 + 2^{-N})]^{-1/2}$.

Note that while it may appear that there is no distance dependence whatsoever to the strength of the effective interaction between qubits, this is not the case. Indeed, as required by causality, the strength of the coupling g of the cavity mode to the qubits scales like $1/\sqrt{V}$ where V is the quantization volume of the cavity. For the sizes of systems we consider here, this is not an issue, but ultimately would impose a limitation to performing interactions between qubits in arbitrarily large arrays.

B. Syndrome extraction

Measuring stabilizers of a quantum error correcting code is the most vital step during quantum error correction. We need an efficient, and fault-tolerant syndrome extraction circuit so that errors arising during the syndrome extraction doesn't spread into data qubits. In addition to being fault-tolerant, the process should be highly parallelizable and fast to prevent backlog issues [19]. We briefly review Shor's method of syndrome extraction before discussing the DiVincenzo-Aliferis method.

1. Shor's method

The circuit shown in Fig. 2 follows Shor's method [29] for stabilizer measurement. The steps involved are,

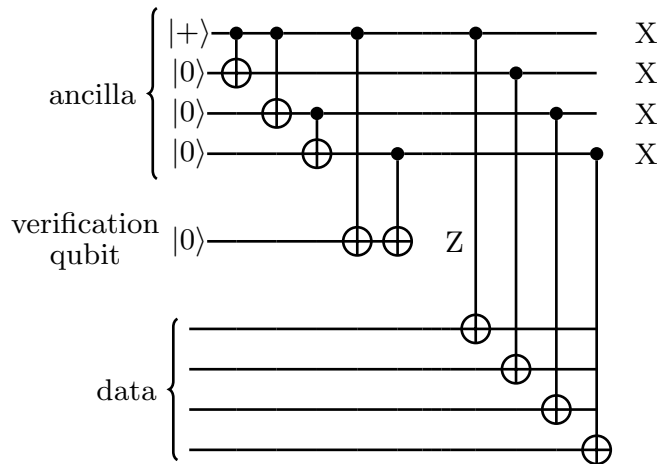


FIG. 2. Circuit representing Shor's style of fault-tolerant syndrome extraction for $[[7, 1, 3]]$ Steane code where a verification qubit measures the parity $Z_1 Z_4$. An outcome of +1 indicates the ancilla is error-free, while -1 signals an error in ancilla preparation, requiring the batch to be discarded and preparation re-attempted.

1. Prepare the ancilla qubits in a classical repetition code or "cat" state.
2. Verify the cat state.
3. Apply CNOT gates coupling the ancilla and data qubits.
4. Measure the ancilla qubits to obtain the stabilizer measurement outcome or syndromes.

These steps are repeated for all stabilizers to collect syndromes, which are then fed into a classical decoding algorithm. The decoder outputs a correction operator if the error is correctable, or identifies a logical error if it is not. The verification step is time-intensive and introduces idling errors (or wait errors) on data qubits. This reduces the code's ability to protect the logical information.

2. DiVincenzo-Aliferis method

In 2007, David P. DiVincenzo and Panos Aliferis [28] introduced a novel method of syndrome extraction in which ancilla verification can be bypassed and replaced with a decoding step. While skipping verification may result in the accumulation of errors, these errors can still be detected and corrected after decoding and measurement. The purpose of the decoder is to identify and invert any multi-qubit errors introduced by the encoder and propagated to the data. If the decoder itself is faulty, an additional decoder, referred to as 'redundification of decoding', can be employed to distinguish between errors arising from the decoding process and those originating in other parts of the circuit. Although there are multiple

ways to implement the procedure of skipping verification and post-processing after ancilla-data CNOT operations, DiVincenzo and Aliferis suggest that using a decoder is likely the most efficient approach [28]. This method is particularly beneficial when measurement processes are slow, as it removes the need for immediate access to measurement outcomes.

This method is fault-tolerant as seen from the following arguments. Consider a case where an error occurs during CNOTs between the ancilla and data qubits. Since CNOT gates are implemented transversally, a single X error in the ancilla cannot cause more than one error in the data block. If a Z error propagates from the data to the ancilla during the CNOT operations, it will be manifested as a measurement error. This measurement error can be corrected by repeating the measurement d times, where d is the code distance, and then majority voting. Consider the case where a single error occurs during the ancilla encoding step. It's possible that more than one error can occur during this step, but still the procedure is fault tolerant. The encoder should be designed so that no logical errors arise at the output from a single error within it, and all first-order single-qubit errors can be detected during the decoding step. We provide a detailed explanation of how the decoder operates for Steane's code in Sec. III. Finally, if a single fault occurs in the decoding step. We need to make sure that errors occurring during decoding are not mistaken for errors from other parts of the circuit. This confusion can arise if errors during encoding and ancilla-data coupling give the same syndrome as errors in decoding. In such cases, we have no way of distinguishing the location of actual error. Thus, the decoder should be carefully designed to avoid such confusion. Another way to solve this confusion is to redundify the decoder and measure both sets of ancilla separately. If the two measurement sets agree, we are assured that whatever error occurred was during encoding. If they don't agree, we will know that an error has occurred during decoding, and that the data qubits are unaffected.

Verification involves measurements prior to the ancilla-data CNOTs, and these measurements take significantly longer compared to the single/two qubit gates or cavity-assisted non-local gates. The DiVincenzo-Aliferis method, even with the additional step of decoding that is not present in Shor's method, is much faster. This is because we use the cavity for decoding, which is much faster than the slow measurement process during verification. Another advantage of this method is that we can manage slow measurements because all the operations are Clifford, allowing us to efficiently track and update our Pauli frame. Since we plan to work with codes with higher weight stabilizers, Shor's method would require multiple non-local CNOT gates during verification. In contrast, the DiVincenzo-Aliferis method only requires non-local resources twice: once for encoding and once for decoding.

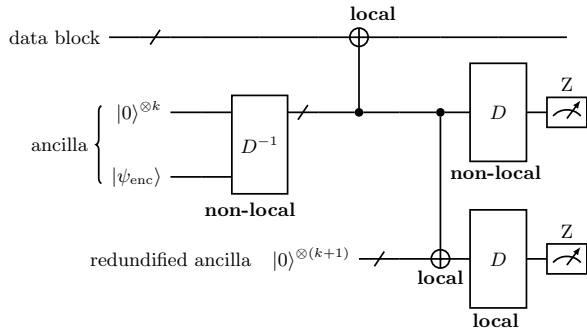


FIG. 3. The circuit illustrates Divincezo-Aliferis style of syndrome extraction circuit. The ancilla is encoded in a GHZ state supported on non-local qubits using cavity, while CNOTs with data are local. Normal decoding is non-local, whereas redundified decoding is local. The measurements of both sets of ancilla qubits are compared to distinguish errors originating from encoding and decoding.

C. Stabilizer quantum codes

Stabilizer quantum codes were introduced by Daniel Gottesman [30] in 1997. Given a stabilizer group S , we can define a subspace H on an N -qubit Hilbert space as the set of all states $|\psi\rangle$ that satisfy $S_i|\psi\rangle = (+1)|\psi\rangle$ for all $S_i \in S$, where $1 \leq i \leq m$. This subspace is called codespace and it defines the quantum stabilizer code C . We use $[[n, k, d]]$ notation for quantum stabilizer codes where n is the number of physical qubits, k is the number of logical qubits and d is the distance of the code. Here, $d(C)$ is defined as the minimum possible weight of a Pauli operator $P \in \Pi^N$ (where $\Pi = \{\pm I, \pm iI, \pm X, \pm iX, \pm Y, \pm iY, \pm Z, \pm iZ\}/\{\pm I, \pm iI\}$ is the equivalence class of Pauli group) that commutes with all the stabilizer generators S_1, \dots, S_m but $P \notin S$. Such Pauli operators are called logical operators.

Stabilizer codes offer significant advantages. One of the key benefits is that, instead of specifying the basis states of the subspace, we can specify the generators of the stabilizer group associated with it. This provides a more compact and convenient representation of the quantum code. Additionally, detecting whether an error has occurred becomes much easier. A Pauli operator $P \in \Pi^N$, where $P \notin S$, is typically interpreted as an *error* that changes the quantum state $|\psi\rangle$ into $P|\psi\rangle$. Such Pauli operators P anti-commute with the stabilizer generators in S , provided they are not logical operators. This indicates that an error has occurred.

1. Quantum Hypergraph product codes (HGP codes)

HGP codes belong to the family of quantum low density parity check codes [31] or qLDPC codes. Given two classical binary codes represented as $[n_1, k_1, d_1]$ and $[n_2, k_2, d_2]$, with their respective parity check matrices H_1 and H_2 , we can use the hypergraph product method introduced by Tillich and Zémor [15] to con-

struct a Calderbank-Shor-Steane (CSS) code [32, 33]. The method involves forming a generator matrix through the combination of two hypergraphs, each aligned with the classical code's parity check matrix. The X and Z stabilizer generators denoted by G_X and G_Z matrices in the symplectic form can be calculated using,

$$\begin{aligned} G_X &= (H_1^T \otimes I_{r_2}, I_{n_1} \otimes H_2), \\ G_Z &= (I_{r_1} \otimes H_2^T, H_1 \otimes I_{n_2}). \end{aligned} \quad (4)$$

Each sublattice block is formed by taking the Kronecker product of two binary matrices, namely $H_1 \in F_2^{r_1 \times n_1}$ and $H_2 \in F_2^{r_2 \times n_2}$, and the Identity matrices denoted by I_{r_i} and I_{n_i} , where $i = 1, 2$. The matrices G_X and G_Z have $r_1 r_2$ and $n_1 n_2$ rows, respectively (some of the rows can be linearly dependent). Both matrices have $N = r_2 n_1 + r_1 n_2$ columns, which determines the block length of the quantum code. The key aspect of this construction is the inherent fulfillment of the commutativity condition, specifically the symplectic product $G_X G_Z^T = 0$. This condition will ensure that all the stabilizers commute with each other.

There are four possible classical codes using the parameters we have defined. The first code, C_1 , has parameters $[n_1, k_1, d_1]$ with its parity-check matrix H_1 . The second code, C_2 , has parameters $[n_2, k_2, d_2]$ and its parity-check matrix is H_2 . Additionally, we can consider the transpose codes: C_1^T , which has parameters $[n_1 - k_1, k_1^T, d_1^T]$ and the parity-check matrix H_1^T , and C_2^T , which has parameters $[n_2 - k_2, k_2^T, d_2^T]$ with the parity-check matrix H_2^T . The resulting quantum code is: $[[n_1 n_2 + (n_1 - k_1)(n_2 - k_2), k_1 k_2 + k_1^T k_2^T, \min(d_1, d_2, d_1^T, d_2^T)]]$. We call qubits belonging to part $n_1 n_2$ as sector-1 qubits and, qubits belonging to part $(n_1 - k_1)(n_2 - k_2)$ as sector-2 qubits. $k_1 k_2$ number of logical qubits are entirely supported on sector-1 qubits, and the remaining $k_1^T k_2^T$ logical qubits are entirely supported on sector-2 qubits.

We can select two parity check matrices at random, each associated with a classical code, and use the hypergraph product shown in Eq. 4 to create a quantum CSS code. If the original parity check matrices have low density or sparsity, the classical codes they represent are LDPC codes [31, 34]. When we use sparse parity check matrices in the hypergraph product, the resulting parity check matrix for the quantum CSS code also remains sparse, leading to a quantum LDPC code or qLDPC code. For example, the parity check matrices corresponding to repetition code are sparse, and the hypergraph product of a repetition code with itself gives a qLDPC code, popularly known as Surface code. For more details on code construction, refer to Appendix B.

III. ERROR ANALYSIS OF STEANE CODE

Steane's $[[7, 1, 3]]$ quantum code [35] is the smallest CSS code [36] that encodes a single logical qubit using

seven physical qubits. This distance-three code can correct one X or Z error and detect two errors on any one of the seven qubits. Being the smallest code in the CSS code family, Steane's code is the easiest to analyze theoretically, and we can attempt to generalize the results to other members of the family.

We start with the N -qubit ancilla state initialized in the all-zero state (represented as all spins down), which resides in the Dicke subspace of a 2^N -dimensional Hilbert space. In the collective angular momentum basis, this state is expressed as $|J = \frac{N}{2}, m_z = -\frac{N}{2}\rangle$, where N is the total number of spin- $\frac{1}{2}$ particles, J is the total angular momentum, and m_z is the projection of angular momentum along the Z -axis. Note that we use a convention that: $|0\rangle = |\downarrow\rangle = |\text{spin} = -\frac{1}{2}\rangle$ and $|1\rangle = |\uparrow\rangle = |\text{spin} = \frac{1}{2}\rangle$. In the case of Steane's code, $N = 4$, but the method described is applicable for any value of N . The encoding of the combined ancilla state into the GHZ state is accomplished in three steps:

1. We apply $e^{-i\frac{\pi}{2}\hat{J}_y}$, which rotates each qubit by an angle of $\frac{\pi}{2}$ about the y -axis, transforming the state to $|+\rangle^{\otimes N}$.
2. We then apply the map \mathcal{E}_{eff} generated by \hat{H}_{eff} as defined in Eq. 2. In the absence of noise, this transformation is unitary and is denoted it \hat{U} .
3. We apply the inverse of the first operation which is $e^{i\frac{\pi}{2}\hat{J}_y}$.

The operations 1-2-3 collectively constitute the encoding process, \hat{E}_D^{-1} , referred to as the 'encoder'. In the absence of noise the encoder is a unitary map and is given by,

$$\begin{aligned} \hat{E}_D^{-1}(\rho) &= e^{i\frac{\pi}{2}\hat{J}_y} \hat{U} e^{-i\frac{\pi}{2}\hat{J}_y} \rho e^{i\frac{\pi}{2}\hat{J}_y} \hat{U}^\dagger e^{-i\frac{\pi}{2}\hat{J}_y} \\ &= \hat{U}_E \rho \hat{U}_E^\dagger. \end{aligned} \quad (5)$$

The next step involves ancilla-data CNOTs, followed by the decoder $\hat{E}_D(\rho) = \left(\hat{E}_D^{-1}(\rho)\right)^\dagger$, and finally ancilla measurement.

As discussed above, the cavity introduces errors due to losses, which alter the cooperativity C , making the map \mathcal{E} given in Eq. 2 no longer unitary. Consequently, our encoding and decoding operations may become faulty. We will examine four different scenarios: (a) perfect encoding & perfect decoding; (b) imperfect encoding & perfect decoding; (c) perfect encoding & imperfect decoding; (d) imperfect encoding & imperfect decoding. Out of this we do not consider case (d) as this would be a second order error.

A. Perfect encoding and perfect decoding

As discussed earlier, in the absence of any losses, both encoding and decoding operations are unitary. The uni-

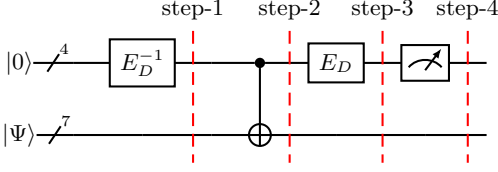


FIG. 4. The circuit illustrates perfect encoding and perfect decoding. The single ancilla here actually represents a set of 4 ancilla qubits, while the single data represents 7 data qubits.

tary, \hat{U} , generated by \hat{H}_{eff} is given by, $\hat{U} = e^{-i\frac{\pi}{2}\hat{J}_z^2}$. The encoder unitary as defined in Eq. 2 is then $\hat{U}_E = e^{i\frac{\pi}{2}\hat{J}_y} e^{-i\frac{\pi}{2}\hat{J}_z^2} e^{-i\frac{\pi}{2}\hat{J}_y} = e^{-i\frac{\pi}{2}\hat{J}_x^2}$. We start with the state $|2, -2\rangle$. After encoding, the state of ancilla becomes,

$$\begin{aligned} \rho_{\text{GHZ}} &= \hat{U}_E |2, -2\rangle \langle 2, -2| \hat{U}_E^\dagger \\ &= \frac{1}{2} \left(|2, 2\rangle + i |2, -2\rangle \right) \left(\langle 2, 2| - i \langle 2, -2| \right) \end{aligned} \quad (7)$$

At this point, the combined (ancilla + data) state is $v_1 = \rho_{\text{GHZ}} \otimes |\Psi\rangle \langle \Psi|$. The next step, as shown in Fig. 4, involves ancilla-data CNOT gates, represented by \hat{V} . We define $\hat{M} = \hat{X}_4 \hat{X}_5 \hat{X}_6 \hat{X}_7$, which is one of the X-stabilizers of the Steane code. Note that \hat{M} can be generalized to represent any stabilizer of either X or Z type. For Z type, the CNOTs will be replaced by CZs. Let's denote $|\psi\rangle \langle \psi|$ by σ for concise notation. The state after step 2 is,

$$\begin{aligned} v_2 &= \hat{V} \left(\rho_{\text{GHZ}} \otimes \sigma \right) \hat{V}^\dagger \\ &= \frac{1}{2} \left(|2, 2\rangle \langle 2, 2| \otimes M \sigma M + |2, -2\rangle \langle 2, -2| \otimes \sigma \right. \\ &\quad \left. + i |2, 2\rangle \langle 2, -2| \otimes M \sigma - i |2, -2\rangle \langle 2, 2| \otimes \sigma M \right). \end{aligned} \quad (8)$$

Next is the decoding step, which is represented by the map $\hat{E}_D \otimes \hat{I}$. After the decoding step, the state is

$$\begin{aligned} v_3 &= (\hat{U}_E^\dagger \otimes \hat{I}) v_2 (\hat{U}_E \otimes \hat{I}) \\ &= \frac{1}{2} \left(\underbrace{|2, 2\rangle \langle 2, 2| \otimes (I + M) \sigma (I + M)}_{\text{Contributes to measurement}} \right. \\ &\quad \left. + \underbrace{|2, -2\rangle \langle 2, -2| \otimes (I - M) \sigma (I - M)}_{\text{Contributes to measurement}} \right. \\ &\quad \left. + i \underbrace{|2, -2\rangle \langle 2, 2| \otimes (M - I) \sigma (M + I)}_{\text{Doesn't contribute to measurement}} \right. \\ &\quad \left. + i \underbrace{|2, 2\rangle \langle 2, -2| \otimes (I + M) \sigma (I - M)}_{\text{Doesn't contribute to measurement}} \right). \end{aligned} \quad (9)$$

The final step involves measuring the ancilla. The expectation value of an operator \hat{O} in a state ρ is given by $\text{Tr}(\rho \hat{O})$. When ρ is expanded in the eigenbasis of the

measurement operator, the cross terms do not contribute to the expectation value. Thus, only the diagonal terms contribute to the expectation value because we perform individual Z measurements. The coefficients of these terms represent error syndromes. For example, if we measure Z and find the ancilla in the state $|2, -2\rangle \langle 2, -2|$, it indicates that our data has been projected into the '-1' eigenbasis of M , thus indicating an error.

B. Imperfect encoding and perfect decoding

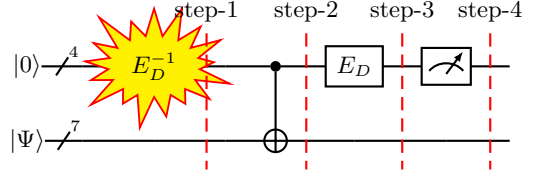


FIG. 5. The circuit illustrates noisy encoding with perfect decoding. The single ancilla here actually represents a set of 4 ancilla qubits, while the single data represents 7 data qubits.

Now, we examine the case of imperfect encoding. The encoder is now a non-unitary map that has decay terms represented by the third term, $\left(\frac{(m-m')^2 i \theta}{\sqrt{C} d_N} \right)$ in Eq. 3. For the case of Steane's code $N = 4$, but the map can be applied to more general cases as well. Before analyzing the imperfect encoding case, we approximate the effect of the encoding map to first order. Here, \mathcal{E}_{eff} , given in Eq. 2 represents the mapping of the state $\rho = \sum_{m, m'} \rho_{m, m'} \left| \frac{N}{2}, m \right\rangle_x \left\langle \frac{N}{2}, m' \right|_x$ under the evolution of H_{eff} , given in Eq. 1.

$$\begin{aligned} \mathcal{E}_D^{-1}(\rho) &= e^{i\frac{\pi}{2}\hat{J}_y} \mathcal{E}_{\text{eff}} \left(e^{-i\frac{\pi}{2}\hat{J}_y} \rho e^{i\frac{\pi}{2}\hat{J}_y} \right) e^{-i\frac{\pi}{2}\hat{J}_y} \\ &= \sum_{m, m'} \rho_{m, m'} e^{i\theta_{-m, -m'}} \left| \frac{N}{2}, m \right\rangle_x \left\langle \frac{N}{2}, m' \right|_x. \end{aligned} \quad (10)$$

Here $\left| \frac{N}{2}, m \right\rangle_x$ is a short hand notation for $\left| J = \frac{N}{2}, m_x = m \right\rangle$, which is the state with the projection of angular momentum along the x-axis is m , and $\theta_{m, m'}$ is defined in Eq. 3. The map can be split into unitary and non-unitary part. After Taylor expanding the non-unitary part we obtain,

$$\begin{aligned} \mathcal{E}_D^{-1}(\rho) &= \sum_{q, r, s=0}^{\infty} (-2)^s \alpha^{(q+r+s)} \frac{1}{q! r! s!} \\ &\quad \times \hat{J}_x^{(s+2q)} \hat{E}_D^{-1}(\rho) \hat{J}_x^{(s+2r)}. \end{aligned} \quad (11)$$

with $\alpha = \left(\frac{\theta}{\sqrt{C} d_N} \right)$. For large C we only keep terms with $q + r + s \leq 1$,

$$\mathcal{E}_D^{-1}(\rho) \approx \tau + \frac{2\theta}{\sqrt{C}d_N} \hat{J}_x \tau \hat{J}_x - \frac{\theta}{\sqrt{C}d_N} \left(\hat{J}_x^2 \tau + \tau \hat{J}_x^2 \right), \quad (12)$$

where $\tau = \hat{E}_D^{-1}(\rho)$ is the output of perfect encoding. We have the following relations from angular-momentum algebra,

$$\hat{J}_x = \frac{\hat{J}_+ + \hat{J}_-}{2} \quad (13)$$

$$\hat{J}_x^2 = \hat{J}_+^2 + \hat{J}_-^2 + \hat{J}_+ \hat{J}_- + \hat{J}_- \hat{J}_+. \quad (14)$$

The terms $\hat{J}_x^2 \tau + \tau \hat{J}_x^2$ will not contribute to the final measurement. We can expand the terms in angular momentum basis as,

$$\langle m | \hat{J}_x^2 \rho | m \rangle = \langle m | (\hat{J}_+^2 + \hat{J}_-^2 + \hat{J}_+ \hat{J}_- + \hat{J}_- \hat{J}_+) \rho | m \rangle. \quad (15)$$

The terms $\langle m | (\hat{J}_+^2 + \hat{J}_-^2) | m \rangle$ will not contribute to the diagonals. The leftover term: $(\hat{J}_+ \hat{J}_- + \hat{J}_- \hat{J}_+)$ can be rewritten as, $(\hat{J}^2 - \hat{J}_z^2)$ and this term keeps the GHZ state invariant as shown below,

$$\langle m | (\hat{J}^2 - \hat{J}_z^2) | m \rangle = J(J+1) \langle m | \rho | m \rangle - \langle m | \hat{J}_z^2 \rho | m \rangle. \quad (16)$$

Since \hat{J}^2 preserves the angular momentum basis and \hat{J}_z^2 terms are undetectable in the final Z-basis measurement, the omitted terms in the simulation, despite their complexity are harmless and do not impact the results.

In calculations below, v again denotes the state without noise, and \tilde{v} denotes the state with noise. Now, we will go through each steps of the circuit shown in Fig. 5:

We start with the ancilla in all-zero state. After encoding, which is step 1, the ancilla is in the state $\rho_{\text{GHZ}} + \hat{J}_x \rho_{\text{GHZ}} \hat{J}_x$, where ρ_{GHZ} is the perfect GHZ state as defined in Eq. 7, and \hat{J}_x represents the sum of single-qubit bit-flip errors on each ancilla qubit, as described in Eq. 18. The combined state after step 1 is,

$$\tilde{v}_1 \approx (\rho_{\text{GHZ}} + \frac{2\theta}{\sqrt{C}d_N} \hat{J}_x \rho_{\text{GHZ}} \hat{J}_x) \otimes \sigma. \quad (17)$$

Where $\sigma = |\psi\rangle\langle\psi|$ is the state of the data qubits and other parameters are as defined in Eq. 3. Let us also define the probability of error to be $p_e = \frac{2\theta}{\sqrt{C}d_N}$.

Step 2 is ancilla-data CNOTs. From case A we know how ρ_{GHZ} transforms after this step. Now we need to determine the transformation of $\hat{J}_x \rho_{\text{GHZ}} \hat{J}_x$. Instead of directly calculating the transformation of $\hat{J}_x \rho_{\text{GHZ}} \hat{J}_x$, we can track the transformation of the operator \hat{J}_x and then apply to v_2 , the state obtained in the absence of noise. To distinguish between Pauli operators acting on ancilla and data qubits, we will use X_i for Pauli-X acting on

ancilla qubits and X'_i for Pauli-X acting on data qubits. Using this notation \hat{J}_x is given by,

$$\hat{J}_x = \frac{1}{2} \left(\hat{X}_1 \hat{I}_2 \hat{I}_3 \hat{I}_4 + \hat{I}_1 \hat{X}_2 \hat{I}_3 \hat{I}_4 + \hat{I}_1 \hat{I}_2 \hat{X}_3 \hat{I}_4 + \hat{I}_1 \hat{I}_2 \hat{I}_3 \hat{X}_4 \right). \quad (18)$$

We know how an X error propagates through a CNOT gate (see appendix A for details). The \hat{J}_x operator spreads the X error bit-wise to the data qubits according to the circuit shown in Fig. 5. If we denote the four CNOT operations as \hat{V} , we get,

$$\hat{\mathcal{X}} = \hat{V} \left\{ \hat{J}_x \otimes \mathbb{1} \right\} \hat{V}^\dagger = \frac{1}{2} \left(\hat{X}_1 \hat{X}'_7 + \hat{X}_2 \hat{X}'_6 + \hat{X}_3 \hat{X}'_5 + \hat{X}_4 \hat{X}'_4 \right) \quad (19)$$

the state after this step becomes:

$$\begin{aligned} \tilde{v}_2 &\approx \hat{V} \tilde{v}_1 \hat{V}^\dagger \\ &= \hat{V} \left((\rho_{\text{GHZ}} + p_e \hat{J}_x \rho_{\text{GHZ}} \hat{J}_x) \otimes \sigma \right) \hat{V}^\dagger \\ &= v_2 + p_e \hat{V} \left(\hat{J}_x \otimes \mathbb{1} \right) \hat{V}^\dagger v_2 \hat{V} \left(\hat{J}_x \otimes \mathbb{1} \right) \hat{V}^\dagger \\ &= v_2 + p_e \hat{\mathcal{X}} v_2 \hat{\mathcal{X}}^\dagger \end{aligned} \quad (20)$$

Step 3 is the decoding step. Since we are considering the case of perfect decoder, \hat{E}_D transforms the perfect state v_2 to v_3 . So the imperfect state becomes,

$$\begin{aligned} \tilde{v}_3 &\approx (\hat{U}_E \otimes \hat{I}) \left(v_2 + p_e \hat{\mathcal{X}} v_2 \hat{\mathcal{X}}^\dagger \right) (\hat{U}_E^\dagger \otimes \hat{I}) \\ &= (\hat{U}_E \otimes \hat{I}) v_2 (\hat{U}_E^\dagger \otimes \hat{I}) \\ &+ p_e \left[(\hat{U}_E \otimes \hat{I}) \hat{\mathcal{X}} (\hat{U}_E^\dagger \otimes \hat{I}) \right] v_3 \left[(\hat{U}_E \otimes \hat{I}) \hat{\mathcal{X}}^\dagger (\hat{U}_E^\dagger \otimes \hat{I}) \right] \\ &= v_3 + p_e \hat{\mathcal{X}} v_3 \hat{\mathcal{X}}^\dagger. \end{aligned} \quad (21)$$

Here, \tilde{v}_3 represents the imperfect state after step 3, while v_3 denotes the final perfect state from case A as defined in Eq. 9. The last step follows from the fact that \hat{U}_E , which is $e^{i\frac{\pi}{2}\hat{J}_x^2}$, commutes with $\hat{\mathcal{X}}$, i.e., $[\hat{U}_E, \hat{\mathcal{X}}] = 0$. We substitute the terms of v_3 into the above equation and obtain error terms like,

$$\begin{aligned} &\sum X_i |2\rangle\langle 2| X_j \otimes (X'_p + X'_\alpha X'_\beta X'_\gamma) \sigma (X'_q + X'_\delta X'_\epsilon X'_\zeta) \\ &+ X_i |-2\rangle\langle -2| X_j \otimes (X'_p - X'_\alpha X'_\beta X'_\gamma) \sigma (X'_q - X'_\delta X'_\epsilon X'_\zeta) \end{aligned} \quad (22)$$

The indices i and j represent the four ancilla qubits, with $1 \leq i, j \leq 4$. The indices p and q ($1 \leq p, q \leq 7$) denote the data qubits that are connected via CNOTs to the ancilla qubits i and j , respectively. The indices α, β, γ (δ, ϵ, ζ) represent the other three data qubits connected to the remaining three ancilla qubits apart from the one indexed

by i (or j). For example, if $i, j = 1$, then $p = q = 7$ and $\alpha = \delta = 4, \beta = \epsilon = 5, \gamma = \zeta = 6$. Similarly, if $i = 3, j = 2$, then $p = 5, q = 6$ and $\alpha = 4, \beta = 6, \gamma = 7, \delta = 4, \epsilon = 5, \zeta = 7$. We will have 16 terms corresponding to different combinations of ancilla and data qubits.

Final step involves measuring the ancilla qubits. We measure all four ancilla in the Pauli-Z basis, and depending upon the measurement outcome, we collapse into one of 16 possible states. The coefficient of the state in Eq. 22 corresponds to error syndrome. For instance, if we get a measurement outcome of -1 on first qubit and $+1$ for the remaining three, this means we have collapsed to the ancilla state $\hat{X}_1 \hat{I}_2 \hat{I}_3 \hat{I}_4 |2\rangle \langle 2| \hat{X}_1 \hat{I}_2 \hat{I}_3 \hat{I}_4$ ($i = j = 1$). From this information we know that the 7th data qubit has suffered a bit flip.

A general error syndrome looks like the coefficients of the terms in Eq. 22. The coefficients are sum of a single qubit bit-flip and a three qubit bit-flip (which is equivalent to a single bit flip).

The faulty encoder, to the first order, generates one bit-flip error on any one of the ancilla qubit. Since the interaction with the data is performed using transversal gates, it cannot introduce more than one error in the data block. Furthermore, since bit-flips, X, commute with the perfect decoding operation $e^{-i\frac{\pi}{2}J_x^2}$, this error syndrome can be detected, and the affected data qubits can be corrected accordingly.

The remaining case is perfect encoding and imperfect decoding. We can follow the same arguments as of imperfect encoding. Since the error is only in decoding step we get the final state to be

$$\tilde{v}_3 \approx v_3 + p_e \left(\hat{J}_x \otimes \mathbb{1} \right) v_3 \left(\hat{J}_x \otimes \mathbb{1} \right) \quad (23)$$

Here the error terms will look like

$$\begin{aligned} & \sum X_i |2\rangle \langle 2| X_j \otimes (\mathbb{I} + M) \sigma (\mathbb{I} + M) \\ & + X_i |-2\rangle \langle -2| X_j \otimes (\mathbb{I} - M) \sigma (\mathbb{I} - M), \end{aligned} \quad (24)$$

and other cross terms. In this scenario, the error can be identified through ancilla measurements and resolved using majority voting. No correction is needed, as the error occurred after the interaction between the ancilla and data qubits, leaving the data qubits unaffected.

C. Fault tolerant analysis

We will now present the following arguments, supported by calculations from previous sections, to demonstrate that our setup is fault-tolerant under these two conditions. We observe that the key element in proving the Fault-Tolerance (FT) for the DiVincenzo-Aliferis method lies in the careful design of the decoding circuit. Specifically, the decoder must be designed so that no single fault within it produces the same syndrome as

any multi-qubit error caused by a single fault in the encoder. Such a decoder can always be constructed for any distance-3 code [28]. However, in our case, since the encoding and decoding operations are performed collectively, the error propagation is more complex.

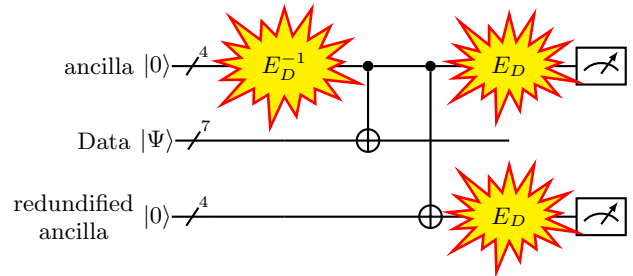


FIG. 6. The circuit illustrates noisy encoding and decoding, where ‘ancilla’ and ‘redundified ancilla’ each represent four qubits. The ancilla is used for stabilizer measurement, while the redundified ancilla is for redundification during decoding. Both sets undergo faulty decoding (E_D), are measured separately in the Z-basis, and their results are compared to isolate errors from the encoding and decoding processes [28].

As discussed in Sec. IIIB our encoder/decoder, to a first-order approximation, can introduce at most a single bit-flip error on any one of the ancilla qubit. In order to demonstrate that the DiVincenzo-Aliferis method remains fault-tolerant with the use of this gate, we must show that any first-order errors cannot result in more than one error within the data qubits.

An important aspect to ensure the fault-tolerance of our protocol is the ability to distinguish errors originating from the encoding process and those from the decoding operations. To do that, we redundify the decoding operation. By repeating the decoding operations and analyzing the syndromes measured after the two decoders, we can confidently determine whether the detected bit-flip errors, to first-order, originated in the encoding or the decoding part. In cases where the decoding is faulty and the syndromes for the bit-flip errors at the two decoding blocks disagree, we can conclude that the error, to first-order, occurred in one of the decoding blocks, leaving the data block unaffected [28]. In this scenario, no correction or recovery operations are needed for the data block. Conversely, if the syndromes agree, it indicates that the detected errors, if any, to first-order, occurred either during the encoding or the ancilla-data CNOTs, both of which could affect the data.

The situation becomes complex when a fault occurs in any of the transversal CNOT gates. The transversal operation can introduce at most one error in the data. The challenge arises when a fault in CNOT gate generates an error that after propagating through the decoder, results in a syndrome overlapping with those caused by an error in the encoder. In this case, the corresponding correction or recovery operation might inadvertently introduce an additional error, resulting in two errors in the data and

compromising fault tolerance. Fortunately, any bit-flip error (X) commutes with the decoding operation, allowing it to remain on the same qubit without causing ambiguity. The real issue arises when Z or Y errors occur during ancilla-data CNOT operations, as these do not commute with the decoder. Such errors can propagate to other ancilla qubits, resulting in syndrome ambiguity. However, after carefully analyzing the commutation relationships between phase errors, Z , bit-and-phase errors, Y , and the decoding operation, we find that single, Z or Y errors propagate through the decoder as follows: $ZIII \leftrightarrow -YXXX$ and $YIII \leftrightarrow ZXXX$, producing distinct error syndromes and reducing the likelihood of ambiguity. In our case, in addition to considering the parity of the measurement outcomes, the outcome of each physical measurement is crucial for accurately locating the error, as explicitly demonstrated in Sec. III B.

We have demonstrated that the DiVincenzo-Aliferis method is fault-tolerant in the three scenarios discussed above. The fourth scenario, involving both imperfect encoding and decoding, is a p^2 event, and therefore we omit a detailed analysis. We conducted numerical simulations using the Steane code, comparing ancilla verification on one side with the DiVincenzo-Aliferis method on the other. Our results show that the DiVincenzo-Aliferis method performs slightly better than ancilla verification, aligning with previous findings [37].

IV. ERROR ANALYSIS OF HYPERGRAPH PRODUCT CODES

We will be using circuit in Fig. 3 for measuring stabilizers of hypergraph product code. It's basically the same circuit that we used for Steane's code in last section except that now the ancilla will be encoded in a weight- w GHZ or "cat" state where w is the weight of X or Z stabilizer generator. Note that the weights of all the stabilizer for these codes are not the same. They keep varying between two integers determined by the choice of check polynomial $h(x)$. We use cavities to simulate non-local gates for the preparation of weight- w GHZ state, while CNOTs between ancilla and data are kept local using our tri-layer arrangement shown in Fig. 9. Normal decoding is non-local, whereas redundified decoding is kept local. The measurement of both sets of ancilla qubits are compared to distinguish errors originating from encoding and decoding steps. The basic unit of the circuit is the physical qubits, which is prone to a variety of errors depending upon the choice of hardware. The types of errors that physical qubits can undergo in our stabilizer measurement circuit are as follows:

1. *Imperfect reset*: Error occurred when a data/ancilla qubit is initialized in $|1\rangle$ instead of $|0\rangle$. This happens with some probability p_{in} (similarly for $|+\rangle/|-\rangle$ state).
2. *Cavity error*: on using cavity or non-local resource

to prepare a state $|\psi\rangle$, we get the perfect state $|\psi\rangle$ with some probability $(1 - p_{\text{cavity}})$ and sum of single bit flip errors $\sum_i^n X_i$, $1 \leq i \leq n$, (where i indicates the qubit on which bit-flip is acting and n denotes the number of qubits participating in gate) with probability p_{cavity} . The failing probability $p_{\text{cavity}} \propto 1/\sqrt{C}$, where C is cooperativity of the cavity, given by $C = g^2/\gamma\kappa$. We will approximate this error as a single bit flip occurring randomly at one of the qubits.

3. *Single-qubit gate error*: while doing a single qubit gate, say H we additionally do \hat{X} , \hat{Z} or \hat{Y} operations, each with probability $p_1/3$. This error model is also known as *single-qubit depolarizing noise*.
4. *Two-qubit gate error*: while doing CNOTs between ancilla and data qubits, we additionally do $\hat{I} \otimes \hat{X}$, $\hat{I} \otimes \hat{Y}$, $\hat{I} \otimes \hat{Z}$, $\hat{X} \otimes \hat{I}$, $\hat{X} \otimes \hat{X}$, $\hat{X} \otimes \hat{Y}$, $\hat{X} \otimes \hat{Z}$, $\hat{Y} \otimes \hat{I}$, $\hat{Y} \otimes \hat{X}$, $\hat{Y} \otimes \hat{Y}$, $\hat{Y} \otimes \hat{Z}$, $\hat{Z} \otimes \hat{I}$, $\hat{Z} \otimes \hat{X}$, $\hat{Z} \otimes \hat{Y}$, or $\hat{Z} \otimes \hat{Z}$, each with probability $p_2/15$. This error model is also known as *two-qubit depolarizing noise*.
5. *Measurement error*: While measuring, say an ancilla qubit in \hat{Z} basis, we incorrectly project into wrong state and report a wrong value with some probability p_{meas} .
6. *Wait or Idle error*: While we are doing error-correction rounds, our data qubits are waiting, represented as in identity gate \hat{I} . But instead, performing a single qubit gate \hat{X} , \hat{Z} or \hat{Y} with probability $p_{\text{wait}}/3$.

The numerical simulations we do have combination of these errors. The errors can occur randomly anywhere in the circuit, with no correlation. Such type of error model or noise is called *Markovian noise*. Depending on the hardware, each errors enumerated above can have different values of probabilities. We consider two different models:

- **Hardware-Agnostic Error Model**: This model is independent of specific hardware implementations, assuming all errors except the cavity error occur with the same probability p throughout the circuit. In our numerical simulations, we account for type 1,3,4 and 5 errors with equal probability, while type 6 (idle error) is set to 0. This is justified by the fact that Rydberg atoms have long coherence time compared to the idle time of data qubit [38][39]. So, $p_1 = p_2 = p_{\text{in}} = p_{\text{meas}} = p$, and $p_{\text{wait}} \approx 0$.
- **Custom Error Model**: In this model, type 4 errors (two-qubit depolarizing) have probability p and type 3 errors (single-qubit depolarizing) have probability $p/10$. Type 5 errors (measurement) and type 1 errors (imperfect reset) each have a probability of $2p$. Type 6 errors (wait) are again set to

0. So, $p_2 = p$, $p_1 = p/10$, $p_{\text{in}} = p_{\text{meas}} = 2p$, and $p_{\text{wait}} \approx 0$.

A. Numerical simulation methods

We used the **STIM** software package in python to simulate the circuits [40]. We performed both hardware-agnostic and custom error model simulations as explained in the previous section. To infer how the threshold changes with respect to the cavity's cooperativity, C , we varied the ratio of cavity error to two-qubit depolarizing error (p_{cavity}/p_2). The gate failure probability scales with C as, $p_{\text{cavity}} \propto 1/\sqrt{C}$. Varying the cavity error helps us understand the relationship between the failure probability p_{cavity} and the cavity parameters, and how these variations impact the threshold.

We refer back to the circuit shown in Fig. 3 for stabilizer measurement throughout our simulations. Stabilizers and logical operators were generated using the **bposd** package [41]. We designed the syndrome extraction circuit to be adaptable to any check polynomial $h(x)$, allowing it to generate the corresponding syndrome extraction circuit for the resulting hypergraph product code with d rounds of extraction. Our numerical simulations can accommodate polynomials of arbitrarily high degree, provided sufficient computational resources are available.

We created two exact replicas of the data qubit arrangement for Z (top layer) and X (bottom layer) stabilizers as illustrated in Fig. 9. To prepare a GHZ state for the measurement of X stabilizers, we use the cavity arrangements in bottom layer and apply the gate described in Eq. 5. But due to limitations in **STIM** package, we used **H** and **CNOT** gates and approximated the errors. The dominant error is $\hat{J}_x = \sum_i^n X_i$ with a probability p_{cavity} , where n denotes the number of ancilla qubits involved. We approximate this error by neglecting the cross terms, which results in the error model where a single bit-flip error can happen at random. This is justified by the fact that cross terms do not contribute to the syndrome measurements. To model this error in **STIM**, we used **CORRELATED** and **ELSE_CORRELATED** functions as explained in Appendix D. We then applied **CNOTs** between ancilla and data layers, followed by 2-qubit depolarizing errors. A separate ancilla layer was used for redundification in decoding, applying **CNOTs** and decoding them separately using cavities. We use the same error model as we used for encoding. We measured all ancillas in the Z -basis followed by appropriate measurement errors and repeated the syndrome extraction round d times, where d is the code distance.

In **STIM**, stabilizer generators cannot be directly declared. Instead, the set of deterministic measurements that determine the stabilizer outcome (either '0' or '1') are passed into a function called **DETECTORS**. We initialize all data and ancilla qubits in the zero state, and for each X and Z stabilizer, we begin by declaring the corresponding **DETECTORS**. Two types of detectors were used in our

simulations: (i) tracking errors across time by **XORing** the current and previous round of ancilla measurements, and (ii) local detectors **XORing** measurements of both ancilla sets to distinguish between encoding and decoding errors. As mentioned above, we perform d rounds of error correction, where d is the code distance. Following the declaration of stabilizers, we specify the set of logical observables of interest using the **OBSERVABLE_INCLUDE** function. Since we initialize the data qubits in the all-zero state, after the projective stabilizer measurements, the system is projected into the logical zero state, $|0\rangle_L$, subspace of the codespace. At this point, the logical- Z observables are deterministic. We then measure all logical- Z observables, and if any of them have flipped, it indicates the occurrence of a logical- X error. **STIM** then generates space-time graph of the entire circuit, where nodes represent detectors and edges correspond to error mechanisms that can trigger these detectors. The space-time graph of d rounds of syndrome extractions is decoded using the sinter integration of the **BP+OSD** decoder [17, 41]. We used the min-sum algorithm for belief propagation, with a maximum of 30 iterations and a scaling factor of 0.625, utilizing a parallel update schedule. If belief propagation fails to converge, its output is sent to **OSD-0** for post-processing. For further details, refer to Appendix . C.

The decoder outputs a correction operator, denoted as c . If $c \notin \text{rowspan}(H)$, meaning the correction operator does not belong to the stabilizer group, it indicates that a logical error has occurred and the decoding attempt has failed. **Sinter** package then perform sampling multiple times to estimate the logical error rate per round for various physical error rate values. This procedure is repeated for the three codes for the same code family. We estimate the threshold of the code family by plotting logical error rate vs physical error rate in log-log scale. The threshold is given by the point where all the codes intersect, and below this point, we observe a sudden change in the slope of all the curves. It means that logical failure rate can be exponentially suppressed once the physical error is below the threshold. Once we have collected sufficient number of sub-threshold data points, we fit all the codes in a code family to the equation [42],

$$P_L(p) = A \left(\frac{p}{p_{th}} \right)^{ad^b}, \quad (25)$$

where $P_L(p)$ represents the logical failure probability per syndrome extraction cycle, calculated as $P_L(p) = 1 - (1 - P_L(p, d))^{1/d}$, with $P_L(p, d)$ being the total logical errors after d rounds of syndrome extraction, and d being the code distance. Here $A, a, b > 0$ and p_{th} is the threshold of a code family under the given error model and decoder. The logical failure probabilities for $p > 10^{-3}$ are determined numerically, after which the data points are fitted to the above equation and extended to $p < 10^{-3}$ to estimate the logical failure rates.

After obtaining the threshold values for different ratios of p_{cavity} to p_2 , as shown in Tab. II, we compute the

corresponding cooperativity of the cavity. Given that $p_{\text{cavity}} = \frac{2N\theta}{\sqrt{C}d_N}$, and denoting the ratio p_{cavity}/p_2 as m , we can rearrange this equation to determine the cooperativity at $p_2 = p_{\text{th}}$. For GHZ state preparation, we have $\theta = \pi/2$ and $d_N = \frac{1}{\sqrt{2(1+2^{-N})}}$ [27], where N is the number of qubits involved in the non-local gates. Thus, the cooperativity C is given by:

$$C = \left(\frac{N\pi}{mp_{\text{th}}\sqrt{2(1+2^{-N})}} \right)^2 \quad (26)$$

Using this relation, we can calculate the cooperativity C for a given value of $p_{\text{cavity}} = mp_{\text{th}}$. This establishes a key relationship between the code performance, represented by p_{th} , and the critical experimental parameter, cooperativity C . Cooperativity C is an essential metric for experimentalists, as it quantifies the quality of coupling between bosonic modes and Rydberg atoms.

B. Simulation Results for $h(x) = 1 + x + x^2$

We used the code generated via check polynomial $h(x) = 1 + x + x^2$, with lift = 6, 9, 12 under periodic boundary conditions. Details of code construction has been discussed in Appendix B, and Table I lists down the codes we get. For this code family, we find numerically that the scaling of the logical error rate in Eq.25 is best fit by the positive constants $a \approx 3/4$, and $b \approx 1$.

Lift	Periodic
6	[[72, 8, 4]]
9	[[162, 8, 6]]
12	[[288, 8, 8]]

TABLE I. Codes generated via check polynomial $h(x) = 1 + x + x^2$ under periodic boundary conditions.

If a cavity has a certain cooperativity, we can expect a corresponding threshold, as listed in the Table II. As the quality of the cavity decreases, the corresponding threshold also reduces, which aligns with our expectations. For example, when the cavity error rate is 10 times the two-qubit depolarizing error rate, $p_{\text{cavity}}/p = 10$, we get a high threshold of approximately 6.09×10^{-3} , or 0.609% and the corresponding cooperativity of around 4.72×10^4 .

We can also use this simulation data to see what level of cooperativity would be needed to achieve a certain logical error rate. Figure 7 shows the plot for various fixed two-qubit error rates. For instance, a fidelity of 99.91% has been achieved for two-qubit entangling gates [43]. If we put this value as p_2 , we can plot the logical failure rate (LFR) achieved for different cooperativity. It can be seen in Fig. 7 that we can achieve 10^{-6} LFR for a cooperativity of around 10^6 . The results improve exponentially as better fidelities are achieved.

Experimentally, implementing codes with periodic boundaries is more challenging than those with open boundaries [25] because interactions which are local on a periodic lattice are highly non-local with open boundaries. However, a key advantage of our cavity setup is that it enables the implementation of periodic boundary codes, doubling the number of logical qubits with only a few additional physical qubits while maintaining the same code distance.

C. Simulation Results for $h(x) = 1 + x + x^3 + x^7$

The true potential of our non-local resource lies in its ability to execute long-range non-local gates with minimal constraints, as discussed previously. This capability enables us to extend our proposal to high-rate codes generated by higher-degree polynomials, which produce highly non-local stabilizers. In this work, we specifically examine codes generated by the check polynomial $h(x) = 1 + x + x^3 + x^7$, as previously explored in [44]. We provide the code specifications, with construction details and the 2D layout in Appendix B.

Since our cavity setup allows for implementing periodic boundary codes, which doubles the number of logical qubits compared to open boundary codes, we will focus on studying periodic boundary codes. Table III shows the different codes that could be generated using this check polynomial. Due to limitations of computational resources, we could only do the simulation for the [[450, 98, 5]] code. See Fig. 8 for the plot of logical error rate per round with the physical error rate. It is not possible to calculate the threshold with simulation from just one member of the code family. However, a pseudo-threshold can be estimated from the plot, which is determined when the logical failure rate intersects with the physical error rate at the $y = x$ line. This point appears to be around $p = 0.0015$, or 0.15%.

V. ARCHITECTURE FOR SYNDROME EXTRACTION CIRCUIT

We propose a 3-dimensional tri-layer architecture for scheduling stabilizer measurements. The top and bottom layers represent ancilla qubits, labeled as ‘ancilla-1’ and ‘ancilla-2’, respectively. The middle layer contains data qubits encoded in the logical space of a hypergraph product code, generated by the check polynomial $h(x)$. Both ancilla layers are exact copies of the data qubit layer. Ancilla-1 is specifically used to measure Z stabilizers, while ancilla-2 is used for the measurement of X stabilizers. Support for both stabilizers in this layout is confined to just one row and one column, simplifying the use of cavity arrangements for GHZ state preparation. We begin by identifying the support of a Z (or X) stabilizer in the data qubits and then select the corresponding set of qubits in ancilla-1 (or ancilla-2) for GHZ

p_{cavity}/p	Threshold	Cooperativity
0.5	7.99×10^{-3}	1.10×10^7
1	7.78×10^{-3}	2.89×10^6
2	6.94×10^{-3}	9.08×10^5
3	6.78×10^{-3}	4.23×10^5
4	5.78×10^{-3}	3.27×10^5
5	5.48×10^{-3}	2.33×10^5
10	5.31×10^{-3}	6.20×10^4

p_{cavity}/p	Threshold	Cooperativity
0.5	8.43×10^{-3}	9.85×10^6
1	8.12×10^{-3}	2.65×10^6
2	7.90×10^{-3}	7.01×10^5
3	7.68×10^{-3}	3.30×10^5
4	7.08×10^{-3}	2.18×10^5
5	6.59×10^{-3}	1.61×10^5
10	6.09×10^{-3}	4.72×10^4

TABLE II. Simulation results for codes with **periodic boundary conditions** under different noise models. The left table presents results under the **custom circuit-level noise model**, while the right table shows results under the **agnostic circuit-level noise model**. In both cases, p_{cavity} represents the error from the imperfect cavity, and p denotes the two-qubit depolarizing error after CNOT operations between ancilla and data qubits. See main text for details about cooperativity calculation. We varied the ratio p_{cavity}/p across the listed (randomly chosen) values to observe threshold variations.

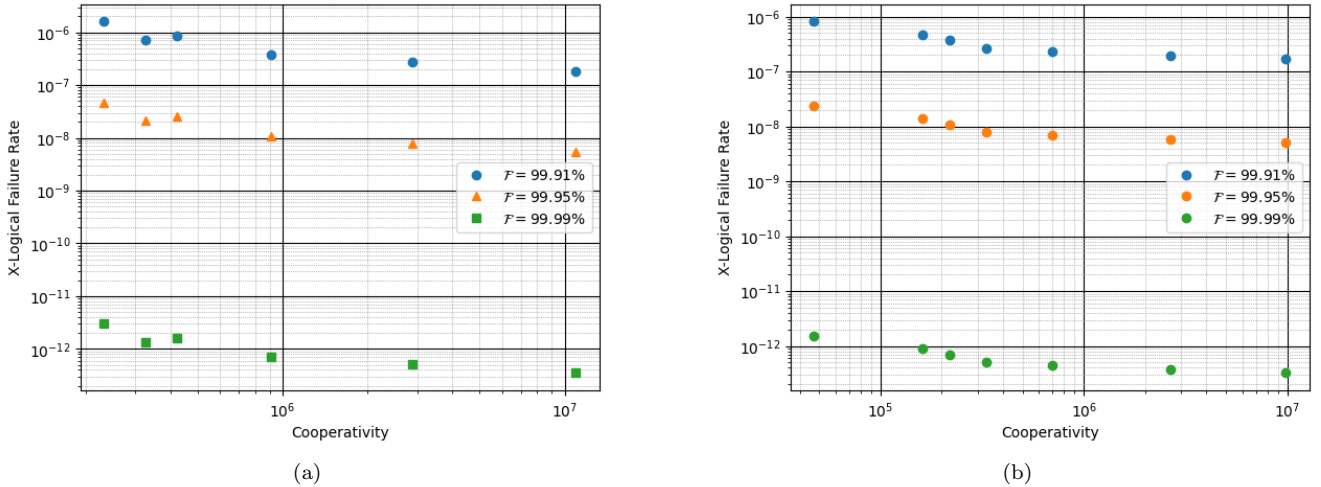


FIG. 7. Plots showing failure rate of logical-X observables Vs cooperativity for $[[288, 8, 8]]$ code under a) Custom noise model and b) Hardware-agnostic noise model.

lift	Codes:Periodic Boundaries
15	$[[450, 98, 5]]$
30	$[[1800, 98, 10]]$

TABLE III. Codes generated via check polynomial $h(x) = 1 + x + x^3 + x^7$ under open and periodic Boundary Condition.

state preparation. Next, CNOT gates are applied between ancilla-1 (or ancilla-2) and the data qubits, which can be performed locally. This is followed by transferring the information from ancilla-1 (or ancilla-2) to another set of ancilla qubits for redundification of the decoding process. Both ancilla sets are then decoded separately, again using the cavity. Finally, both sets of ancilla qubits are measured in the Z basis.

The motivation for proposing a tri-layer architecture is three-fold: first, if the ancilla and data qubits were placed in the same layer, as done in the surface code, spatial congestion would arise due to the use of a w -body $|GHZ\rangle_w$ state (which is $(|0\rangle^w + |1\rangle^w)/\sqrt{2}$) to measure a w -weight stabilizer. The codes listed in Table III have

stabilizers with weight 8. So placing 8 ancilla qubits for each X and Z stabilizer in the same layer would already lead to congestion. While resetting and reusing the same ancilla qubits for different stabilizers is possible, it introduces two significant downsides: reducing the number of stabilizers that can be measured simultaneously, which eliminates the possibility of parallelization, and causing data-ancilla connections for many stabilizers to become non-local and irregular. This will complicate the execution of the CNOT gates even with a cavity setup. Parallelization and locality is essential for improving the efficiency and speed of quantum error correction protocols, as it helps prevent backlog issues and reduces idle errors on data qubits. A tri-layer architecture is a promising solution to achieve these objectives. Second, the stabilizers of hypergraph product codes have support along specific rows and columns. This enables the strategic placement of cavities along these rows and columns, as illustrated in Fig. 9. The tri-layer architecture simplifies the setup by facilitating cavity placement. For each stabilizer measurement, we only need to activate two pairs of cavities: one pair for encoding and another for decoding. And

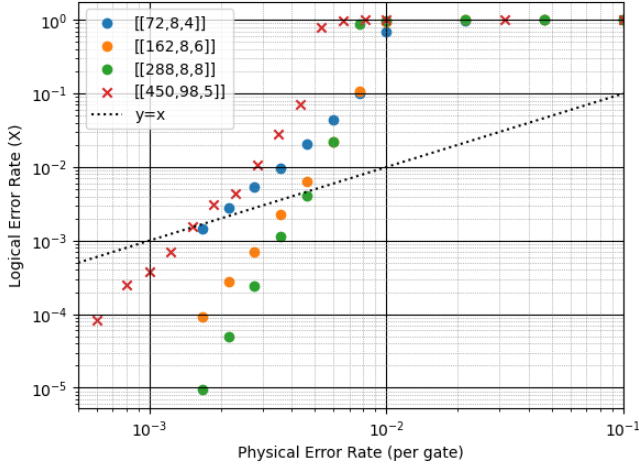


FIG. 8. Plot showing logical-X error rate per syndrome extraction cycle vs. the physical error rate (per gate) for various codes we have simulated. The plots are presented on a log-log scale. The simulations were carried out using STIM, with each data point based on 10^5 Monte Carlo samplings. The fitting lines were obtained using fitting Eq. 25. Here the ratio $p_{\text{cavity}}/p = 1$

finally, the tri-layer setup helps to prevent cross-talk between data and ancilla qubits, a significant issue when everything is confined to a single layer.

To create the $|GHZ\rangle_w$ state, we employ two distinct cavities, referred to as cavity-1 and cavity-2, as depicted in Fig. 10. Let's label the horizontal qubits as h_1, h_2, h_3 and the vertical qubits as v_1, v_2, v_3 . We first use cavity-1 to prepare the GHZ state on the horizontal qubits: $|GHZ\rangle_{h_1 h_2 h_3}$. Then, similarly we use cavity-2 to prepare the GHZ state on the vertical qubits: $|GHZ\rangle_{v_1 v_2 v_3}$. We can then measure the parity between any two horizontal and vertical qubits, such as $Z_{h_3} Z_{v_1}$, to project the system into a combined GHZ state.

$$|GHZ\rangle_{h_1 h_2 h_3} = (|000\rangle_{h_1 h_2 h_3} + |111\rangle_{h_1 h_2 h_3}) \quad (27)$$

$$|GHZ\rangle_{v_1 v_2 v_3} = (|000\rangle_{v_1 v_2 v_3} + |111\rangle_{v_1 v_2 v_3}) \quad (28)$$

Upon measuring $Z_{h_3} Z_{v_1}$, with the measurement outcome m , the combined state $|GHZ\rangle_{h_1 h_2 h_3} \otimes |GHZ\rangle_{v_1 v_2 v_3}$ is projected into the $|GHZ\rangle_6 = (|000, 000\rangle + |111, 111\rangle)/\sqrt{2}$ state if $m = 0$. If $m = 1$, apply the correction $X_{h_1} X_{h_2} X_{h_3}$ or $X_{v_1} X_{v_2} X_{v_3}$ to prepare the $|GHZ\rangle_6$ state. The correction term after measurement can be written as $(X_1 X_2 X_3)^m$.

A. Scheduling stabilizer measurement

As discussed above, we can arrange the physical qubits of a Hypergraph product code so that each X (or Z) stabilizer has support only along a single row and column. As illustrated in Fig. 11, cavities can be positioned along

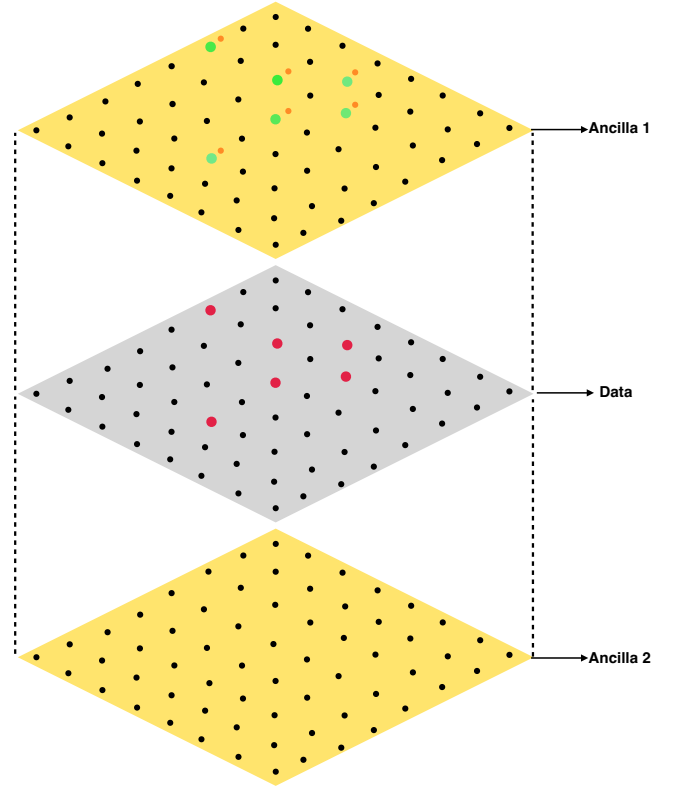


FIG. 9. An illustration of tri-layer architecture for stabilizer measurement. The top and bottom layers contain ancilla qubits, labeled as ancilla-1 and ancilla-2, respectively. The middle layer contains data qubits, which are encoded in the logical space of a hypergraph product code. Qubits shown in red represent the support of a Z stabilizer. Green-colored qubits in ancilla-1 are targeted by the cavity for GHZ state preparation, while orange-colored qubits are used for redundancy of decoding. The same method is applied to the X stabilizers, but this time using ancilla-2.

these rows and columns allowing targeted qubit operations for gate implementation. During a stabilizer measurement, such as a Z type as shown in left hand side of Fig. 11, cavities along its row and column are required. Consequently, no other stabilizer measurement can be performed along the same row and column, as those cavities are already in use. However, we can measure another Z -stabilizer two rows down along the diagonal, as its support does not overlap with the previous stabilizer, thus avoiding any cavity conflict. Similarly, we can proceed downwards along the diagonal. Since we have a separate ancilla layer, ancilla-2, for measuring X -stabilizers, we can proceed in the same fashion. This is shown in the right side of Fig. 11.

Now we use cavities to prepare a GHZ state and proceed with CNOTs between ancilla and data. However, the CNOTs for X and Z stabilizers between ancilla and data must be applied carefully. There are two ways we could think of doing this: i) We can start with an X or Z stabilizer and apply the CNOTs between ancilla and

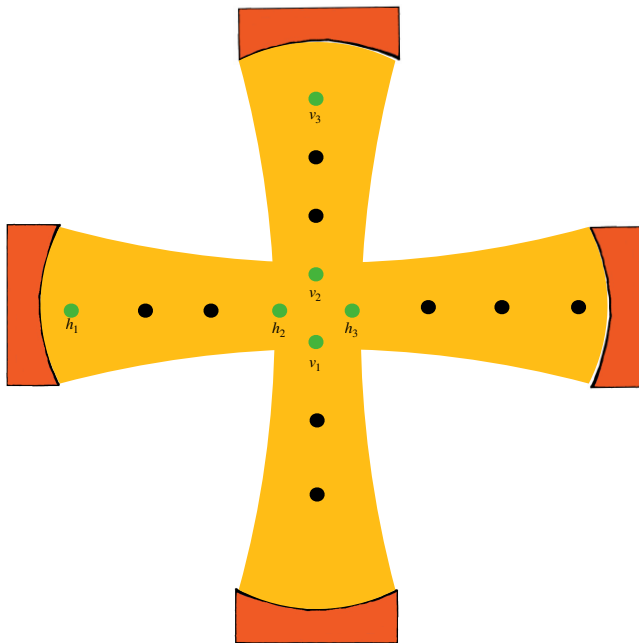


FIG. 10. An illustration of GHZ state preparation using cavities. We use two cavities designated as cavity-1 and cavity-2 to prepare a $|GHZ\rangle_w$ state. Cavity-1 prepares GHZ state on qubits placed horizontally, while cavity-2 prepares GHZ on qubits placed vertically. We can measure parity of any two qubits to project the combined state into $|GHZ\rangle_w$ state.

data in an alternating fashion, i.e., first perform CNOTs for X (or Z), wait until all the CNOTs are done, then perform CNOTs for Z (or X). Continue alternating in this manner. Or ii) We can do all the CNOTs for Z -checks in diagonal in one time-step, and then do all the CNOTs for X -checks in diagonal in another time step.

Mixing the CNOTs of X and Z stabilizers may result in measuring the wrong operator with a global phase of -1 . To avoid this issue, it is best to wait until all the CNOTs of Z (or X) have been applied before proceeding to CNOTs of X (or Z). In a single time step, all stabilizers along a diagonal can be measured. In subsequent time steps, we can move up or down along the anti-diagonal to perform the rest of the stabilizer measurements. This method ensures no cavity overlap and effectively parallelizes the syndrome extraction. For a code $[[2n^2, 2k^2]]$ obtained through the hypergraph product of a classical code $[n, k]$ with itself, all stabilizers can be measured in $2(2n-1)$ time steps. The number of stabilizers measured per time step varies with the number of checks along a diagonal.

VI. CONCLUSION AND OUTLOOK

We have developed an approach for performing QEC for a large class of codes by integrating non-local gates with the DiVincenzo-Aliferis method for stabilizer mea-

surements. By coupling qubits to a cavity, high quality cat states can be deterministically encoded and decoded in one step each. We began with the $[[7, 1, 3]]$ Steane code and analyzed various cases of cavity errors, demonstrating fault tolerance for each scenario. Next, we incorporated the cavity error model into circuit-level noise simulations of the hypergraph product code, achieving a promising threshold, thereby advancing towards large-scale fault-tolerant quantum computing. The STIM circuit we developed for syndrome extraction can be generalized to any generating polynomial $h(x)$ with an arbitrary degree. Our code for producing the syndrome extraction circuit could also be implemented for lifted product codes, which would have a much higher encoding rate than hypergraph product codes [45, 46]. The scheduling approach we present here is also applicable to lifted product codes since they share a similar layout with hypergraph product codes. We plan to extend our simulations to these codes in the future.

We numerically tested the effect of circuit level noise for codes generated by $h(x) = 1 + x + x^2$. For a hardware-agnostic error model, we achieved a threshold ranging between 0.84% – 0.60% for corresponding values of cooperativity in the range $9.85 \times 10^6 - 4.72 \times 10^4$. For the custom error model the threshold values were between 0.8% - 0.53% and the cooperativity ranged from $1.1 \times 10^7 - 6.2 \times 10^4$. A logical failure rate of 10^{-9} can be achieved with a cooperativity of approximately 10^6 , by increasing the two-qubit gate fidelity to 99.96%. However, we struggled to perform simulations for bigger codes which are listed in Table III. We observed the **Sinter** package used for performing Monte-Carlo samplings possibly causes memory leakage. Due to which the memory usage per core starts to increase over time and the code ultimately crashes due to memory error. We tried to sample without using **Sinter** and found the memory usage per core stays constant over time but ends up taking longer time than using **Sinter** package.

We also proposed a tri-layer architecture to efficiently parallelize stabilizer measurements, enabling a complete error correction cycle to be performed in $2(2n-1)$ time steps, where n represents the $[n, k]$ classical code underlying the hypergraph product code. It makes efficient use of the cavity arrangements and also make parallelization of stabilizer measurements possible.

In our setup, performing computations with a $[[N, K, D]]$ code requires $3N$ physical qubits. Recent experimental advancements have demonstrated the ability to control up to 10,000 Rydberg atoms [47]. Allowing for $N \sim 3000$, then using hypergraph product codes, we can achieve $K \sim 100 - 120$ and $D \sim 10 - 15$. We can get even higher encoding rates if we use lifted product codes [45, 46]. The ground state of an $n_x \times n_y$ instance of the Fermi-Hubbard model can be estimated using $2N$ logical qubits, where $N = n_x \times n_y$. With a Rydberg atom quantum computer capable of handling around 100 logical qubits, it is possible to solve at least a 7×7 instance, requiring up to 98 logical qubits [48].

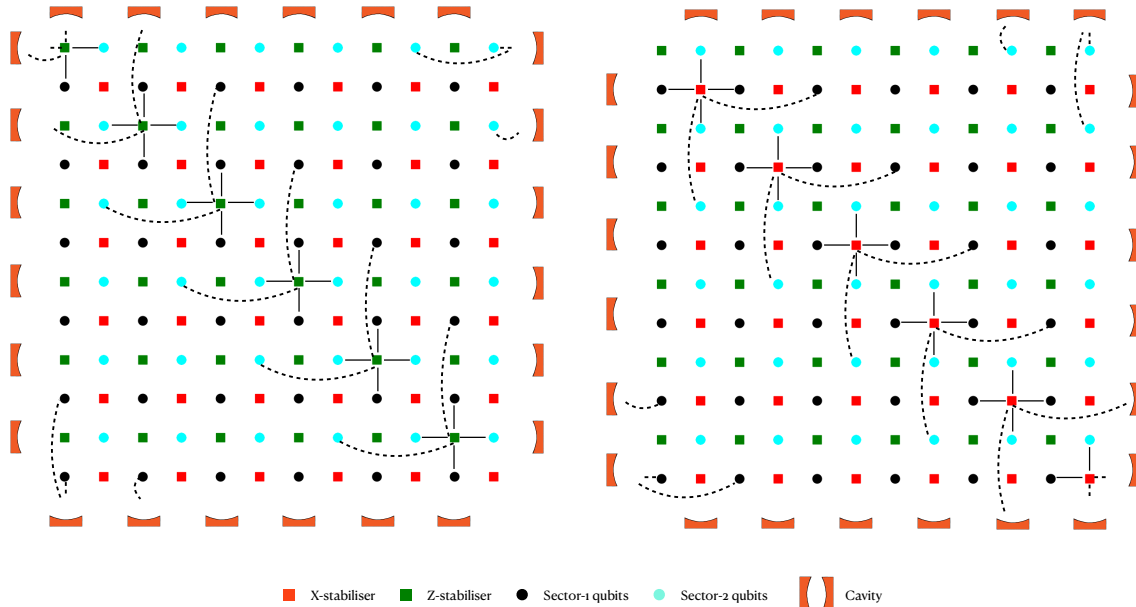


FIG. 11. 2-D layout of $[[72,8,4]]$ code generated via check polynomial $h(x) = 1 + x + x^2$, $\text{lift}=6$ with periodic boundary conditions. (a) Left figure shows GHZ state preparation in ancilla-1 using the non-local resources. Consequently, no other stabilizer measurement can be performed along the same row and column, as the cavities are occupied. However, we can measure another Z-check two unit cells below, as its support does not overlap with the same row or column, thus avoiding any cavity conflict. Similarly, we can proceed downwards along the diagonal. (b) we can proceed in the same fashion in ancilla-2 which we explicitly have for measuring X-checks.

Even though high cooperativity is not available currently in the case of Rydberg atoms in optical cavities, it is potentially possible with microwave cavities. To implement the above-mentioned or other algorithms on a Rydberg atom quantum computer using hypergraph product codes, a fault-tolerant implementation of logical Clifford and non-Clifford gates is required. It is therefore essential to implement a fault-tolerant method for executing logical gates to realize a quantum processor. Moving forward, we plan to investigate the implementation of logical operators using our proposed setup.

VII. ACKNOWLEDGMENTS

We thank Yumang Jing for insightful discussions on cavity error analysis. GKB thanks Guido Pupillo, Sven

Jandura, and Laura Pecorari for many helpful discussions. We also extend our gratitude to Craig Gidney for assistance with STIM-related questions, and to Joschka Roffe and Timo Hillmann for their help with the BPOSD package. OC is supported by Sydney Quantum Academy, Sydney, Australia. We acknowledge support from the Australian Research Council Centre of Excellence for Engineered Quantum Systems (Grant No. CE 170100009). GM and GKB acknowledge funding from BTQ Technologies Corp.

-
- [1] Michele Mosca. *Quantum algorithms*, volume 111. Oxford University Press, 2018.
- [2] Edward Farhi, Jeffrey Goldstone, and Sam Gutmann. A quantum approximate optimization algorithm. *arXiv preprint arXiv:1411.4028*, 2014.
- [3] Ryan Babbush, Dominic W. Berry, Jarrod R. McClean, and Hartmut Neven. Quantum simulation of materi-

- als using scaled symmetry-preserving hamiltonians. *npj Quantum Information*, 4(1):1–7, 2018.
- [4] Yudong Cao, Jonathan Romero, Jonathan P. Olson, Matthias Degroote, Peter D. Johnson, Mária Kieferová, Ian D. Kivlichan, Tim Menke, Borja Peropadre, Nicolas P. D. Sawaya, Sukin Sim, Libor Veis, and Alán Aspuru-Guzik. Quantum chemistry in the age of quantum com-

- puting. *Chemical Reviews*, 119(19):10856–10915, 2019.
- [5] Peter W. Shor. Scheme for reducing decoherence in quantum computer memory. *Physical Review A*, 52(4):R2493–R2496, 1995.
- [6] Raymond Laflamme, Cesar Miquel, Juan Pablo Paz, and Wojciech Hubert Zurek. Perfect quantum error correcting code. *Physical Review Letters*, 77(1):198–201, 1996.
- [7] Alexei Y. Kitaev. Quantum computations: algorithms and error correction. *Russian Mathematical Surveys*, 52(6):1191–1249, 1997.
- [8] Sergey B Bravyi and A Yu Kitaev. Quantum codes on a lattice with boundary. *arXiv preprint quant-ph/9811052*, 1998.
- [9] A Yu Kitaev. Fault-tolerant quantum computation by anyons. *Annals of physics*, 303(1):2–30, 2003.
- [10] Eric Dennis, Alexei Kitaev, Andrew Landahl, and John Preskill. Topological quantum memory. *Journal of Mathematical Physics*, 43(9):4452–4505, 2002.
- [11] Google Quantum AI and collaborators. Quantum computational advantage using a programmable photonic processor. *Nature*, 595:227–232, 2021.
- [12] IBM Quantum team. Demonstration of quantum advantage in machine learning. *npj Quantum Information*, 7(1), 2021.
- [13] Tim H. Taminiau, Julia Cramer, Norbert Kalb, Machiel S. Blok, Loopholes Hensen, Matthew Markham, Daniel J. Twitchen, and Ronald Hanson. Universal control and error correction in multi-qubit spin registers in diamond. *Nature*, 556:491–495, 2018.
- [14] Sergey Bravyi, David Poulin, and Barbara M. Terhal. Trade-offs for reliable quantum information storage in 2d systems. *Physical Review Letters*, 104(5):050503, 2010.
- [15] Jean-Pierre Tillich and Gilles Zémor. Quantum ldpc codes with positive rate and minimum distance proportional to the square root of the blocklength. *IEEE Transactions on Information Theory*, 60(2):1193–1202, 2013.
- [16] Sergey Bravyi, Andrew W Cross, Jay M Gambetta, Dmitri Maslov, Patrick Rall, and Theodore J Yoder. High-threshold and low-overhead fault-tolerant quantum memory. *Nature*, 627(8005):778–782, 2024.
- [17] Joschka Roffe, David R White, Simon Burton, and Earl Campbell. Decoding across the quantum low-density parity-check code landscape. *Physical Review Research*, 2(4):043423, 2020.
- [18] Timo Hillmann, Lucas Berent, Armanda O Quintavalle, Jens Eisert, Robert Wille, and Joschka Roffe. Localized statistics decoding: A parallel decoding algorithm for quantum low-density parity-check codes. *arXiv preprint arXiv:2406.18655*, 2024.
- [19] Luka Skoric, Dan E Browne, Kenton M Barnes, Neil I Gillespie, and Earl T Campbell. Parallel window decoding enables scalable fault tolerant quantum computation. *Nature Communications*, 14(1):7040, 2023.
- [20] M. Saffman, T. G. Walker, and K. Mølmer. Quantum information with Rydberg atoms. *Rev. Mod. Phys.*, 82:2313–2363, 2010.
- [21] Harry Levine, Alexander Keesling, Ahmed Omran, Hannes Bernien, Sylvain Schwartz, Alexander S. Zibrov, Manuel Endres, Markus Greiner, Vladan Vuletic, and Mikhail D. Lukin. High-fidelity control and entanglement of rydberg-atom qubits. *Physical Review Letters*, 121(12):123603, 2018.
- [22] Antoine Browaeys and Thierry Lahaye. Many-body physics with individually controlled rydberg atoms. *Nature Physics*, 16:132–142, 2020.
- [23] Qian Xu, J Pablo Bonilla Ataides, Christopher A Pattison, Nithin Raveendran, Dolev Bluvstein, Jonathan Wurtz, Bane Vasić, Mikhail D Lukin, Liang Jiang, and Hengyun Zhou. Constant-overhead fault-tolerant quantum computation with reconfigurable atom arrays. *Nature Physics*, pages 1–7, 2024.
- [24] Laura Pecorari, Sven Jandura, Gavin K Brennen, and Guido Pupillo. High-rate quantum ldpc codes for long-range-connected neutral atom registers. *arXiv preprint arXiv:2404.13010*, 2024.
- [25] C Poole, TM Graham, MA Perlin, M Otten, and M Saffman. Architecture for fast implementation of qldpc codes with optimized rydberg gates. *arXiv preprint arXiv:2404.18809*, 2024.
- [26] M. Morgado and S. Whitlock. Quantum simulation and computing with Rydberg-interacting qubits. *AVS Quantum Sci.*, 3:023501, 2021.
- [27] Sven Jandura, Vineesha Srivastava, Gavin Brennen, and Guido Pupillo. Non-local multi-qubit quantum gates via a driven cavity, 2023.
- [28] David P. DiVincenzo and Panos Aliferis. Effective fault-tolerant quantum computation with slow measurements. *Phys. Rev. Lett.*, 98:020501, Jan 2007.
- [29] P.W. Shor. Fault-tolerant quantum computation. In *Proceedings of 37th Conference on Foundations of Computer Science*, pages 56–65, 1996.
- [30] Daniel Gottesman. *Stabilizer codes and quantum error correction*. California Institute of Technology, 1997.
- [31] Robert Gallager. Low-density parity-check codes. *IRE Transactions on information theory*, 8(1):21–28, 1962.
- [32] A. R. Calderbank and Peter W. Shor. Good quantum error-correcting codes exist. *Phys. Rev. A*, 54:1098–1105, Aug 1996.
- [33] Andrew Steane. Multiple-particle interference and quantum error correction. *Proceedings of the Royal Society of London. Series A: Mathematical, Physical and Engineering Sciences*, 452(1954):2551–2577, 1996.
- [34] Michael Sipser and Daniel A Spielman. Expander codes. *IEEE transactions on Information Theory*, 42(6):1710–1722, 1996.
- [35] A. M. Steane. Error correcting codes in quantum theory. *Phys. Rev. Lett.*, 77:793–797, Jul 1996.
- [36] A. R. Calderbank and Peter W. Shor. Good quantum error-correcting codes exist. *Phys. Rev. A*, 54:1098–1105, Aug 1996.
- [37] Yu Tomita, Mauricio Gutiérrez, Chingiz Kabytayev, Kenneth R Brown, MR Hutsel, AP Morris, Kelly E Stevens, and G Mohler. Comparison of ancilla preparation and measurement procedures for the steane $[[7, 1, 3]]$ code on a model ion-trap quantum computer. *Physical Review A—Atomic, Molecular, and Optical Physics*, 88(4):042336, 2013.
- [38] M Morgado and S Whitlock. Quantum simulation and computing with rydberg-interacting qubits. *AVS Quantum Science*, 3(2), 2021.
- [39] Mark Saffman, Thad G Walker, and Klaus Mølmer. Quantum information with rydberg atoms. *Reviews of modern physics*, 82(3):2313–2363, 2010.
- [40] Craig Gidney. Stim: a fast stabilizer circuit simulator. *Quantum*, 5:497, 2021.
- [41] Joschka Roffe. Ldpc: Python tools for low density parity check codes. *PyPI* <https://pypi.org/project/ldpc>, 2022.

- [42] Armanda O Quintavalle and Earl T Campbell. Reshape: A decoder for hypergraph product codes. *IEEE Transactions on Information Theory*, 68(10):6569–6584, 2022.
- [43] IQM Quantum Computers. Iqm quantum computers achieves new technology milestones with 99.9% 2-qubit gate fidelity and 1 millisecond coherence time, 7 2024. Press Release.
- [44] Alexey A. Kovalev and Leonid P. Pryadko. Quantum kronecker sum-product low-density parity-check codes with finite rate. *Physical Review A*, 88(1), July 2013.
- [45] Pavel Pantelev and Gleb Kalachev. Quantum ldpc codes with almost linear minimum distance. *IEEE Transactions on Information Theory*, 68(1):213–229, 2021.
- [46] Pavel Pantelev and Gleb Kalachev. Asymptotically good quantum and locally testable classical ldpc codes. In *Proceedings of the 54th Annual ACM SIGACT Symposium on Theory of Computing, STOC 2022*, page 375–388, New York, NY, USA, 2022. Association for Computing Machinery.
- [47] J. C. Bohorquez, R. Chinnarasu, J. Isaacs, D. Booth, M. Beck, R. McDermott, and M. Saffman. Reducing rydberg-state dc polarizability by microwave dressing. *Physical Review A*, 108(2), August 2023.
- [48] Chris Cade, Lana Mineh, Ashley Montanaro, and Stasja Stanisic. Strategies for solving the fermi-hubbard model on near-term quantum computers. *Physical Review B*, 102(23):235122, 2020.
- [49] Armanda O Quintavalle, Paul Webster, and Michael Vasmer. Partitioning qubits in hypergraph product codes to implement logical gates. *Quantum*, 7:1153, 2023.
- [50] David Poulin and Yeojin Chung. On the iterative decoding of sparse quantum codes. *arXiv preprint arXiv:0801.1241*, 2008.
- [51] Nicolas Delfosse and Naomi H Nickerson. Almost-linear time decoding algorithm for topological codes. *Quantum*, 5:595, 2021.
- [52] Pavel Pantelev and Gleb Kalachev. Degenerate Quantum LDPC Codes With Good Finite Length Performance. *Quantum*, 5:585, November 2021.
- [53] Antonio deMarti iOlius, Patricio Fuentes, Román Orús, Pedro M. Crespo, and Josu Etzezarreta Martinez. Decoding algorithms for surface codes. *arXiv preprint arXiv:2307.14989*, 2023.
- [54] Patricio Fuentes, Josu Etzezarreta Martinez, Pedro M Crespo, and Javier Garcia-Frías. Degeneracy and its impact on the decoding of sparse quantum codes. *IEEE Access*, 9:89093–89119, 2021.
- [55] Pavithran Iyer and David Poulin. Hardness of decoding quantum stabilizer codes. *IEEE Transactions on Information Theory*, 61(9):5209–5223, 2015.
- [56] Hanyan Cao, Feng Pan, Yijia Wang, and Pan Zhang. qecgpt: decoding quantum error-correcting codes with generative pre-trained transformers. *arXiv preprint arXiv:2307.09025*, 2023.
- [57] David JC MacKay. Good error-correcting codes based on very sparse matrices. *IEEE transactions on Information Theory*, 45(2):399–431, 1999.
- [58] Sae-Young Chung, G David Forney, Thomas J Richardson, and Rüdiger Urbanke. On the design of low-density parity-check codes within 0.0045 db of the shannon limit. *IEEE Communications letters*, 5(2):58–60, 2001.
- [59] Nithin Raveendran and Bane Vasić. Trapping sets of quantum ldpc codes. *Quantum*, 5:562, 2021.
- [60] Tom Richardson. Error floors of ldpc codes. In *Proceedings of the annual Allerton conference on communication control and computing*, volume 41, pages 1426–1435. The University; 1998, 2003.

Appendix A: Spread of Pauli errors

During the execution of circuit operations, errors will propagate and build up over time. Let’s take the example of a CNOT gate applied to two qubits. As shown in Fig. 12, we can track the evolution of a set of 2-qubit Pauli operators $\{XI, ZI, IX, IZ\}$ under an ideal CNOT operation. In the worst-case scenario, the size of the error doubles. X errors “flow” down a CNOT and Z errors “flow” up. Similarly, CZ gates also propagate errors. However, since these gates are diagonal in the computational basis, they do not impact products of Z operators— $X \otimes I$ transforms into $X \otimes Z$, and $I \otimes X$ becomes $Z \otimes X$.

Appendix B: Details of Code Construction

There are a variety of ways to obtain a sparse parity check matrix. One specific way which we use in this work is through a polynomial. We can define a $n \times n$ circulant matrix \mathbb{X} with entries belonging to field F_q expressed as,

$$\mathbb{X} = \begin{pmatrix} a_0 & a_1 & a_2 & \cdots & a_{n-1} \\ a_{n-1} & a_0 & a_1 & \cdots & a_{n-2} \\ a_{n-2} & a_{n-1} & a_0 & \cdots & a_{n-3} \\ \vdots & \vdots & \vdots & \ddots & \vdots \\ a_1 & a_2 & a_3 & \cdots & a_0 \end{pmatrix}. \quad (\text{B1})$$

Where $a_0, a_1, a_2, \dots, a_{n-1} \in F_q$. A code C is cyclic if $(a_0, a_1, \dots, a_{n-1}) \in C$ implies $(a_{n-1}, a_0, \dots, a_{n-2}) \in C$. Codes that are linear and cyclic can be written in terms of a polynomial $a(x) = a_0 + a_1x + a_2x^2 + \dots + a_{n-1}x^{n-1}$. It is possible to show that any such code consists of a polynomial which is a multiple of a single generator polynomial $g(x)$, which must divide $x^n - 1$. The quotient defines the check polynomial $h(x)$, given by $h(x) = g(x)/x^n - 1$, which is the generator polynomial of the dual code. The degree of the generator polynomial is $\deg g(x) = n - k$, which gives the number of stabilizer generators in the stabilizer group. While the degree of check polynomial $h(x)$ is k , which gives us idea of the number of logical qubits. The classical code corresponding to check polynomial $h(x)$ will have k logical bits. Starting with a generator polynomial $h(x) = a_0x^0 + a_1x^1 + \dots + a_{n-1}x^{n-1}$ of a cyclic code, we can collect the coefficients a_0, a_1, \dots, a_{n-1} and arrange them in matrix form like Eq. B1, and continue to permute the entries into rows below. Now, we can decide the length of the starting vector (or columns of the matrix \mathbb{X}) which we call lift. We provide the following examples for in depth code construction.

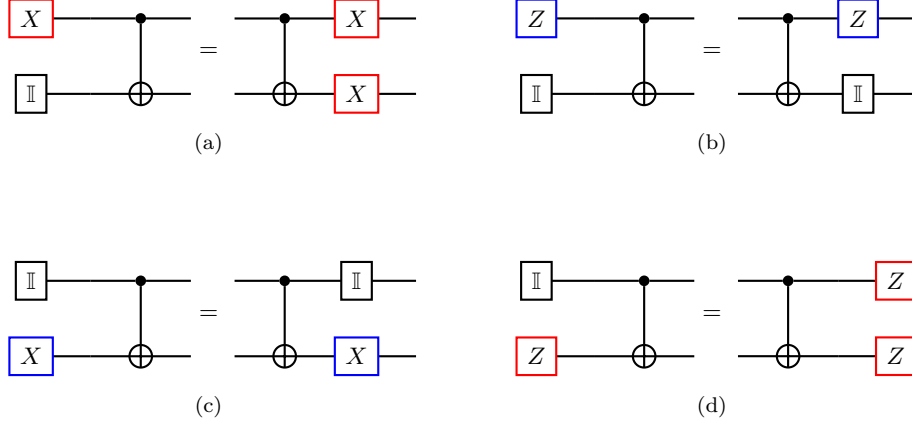


FIG. 12. Error propagation through the CNOT gate. (a) Spread of X error from control qubit to target qubit after CNOT gate. (b) Z error on the control qubit remains unchanged after the CNOT gate. (c) An X error on the target qubit commutes with the CNOT gate. (d) Z error on the target qubit propagates to the control qubit after the CNOT gate.

1. Surface Code from repetition Code

Suppose $h(x) = 1 + x$, so $a_0 = 1$ and $a_1 = 1$. Let the lift be 5. We start with the vector $a_0 = 1, a_1 = 1, a_2 = 0, a_3 = 0, a_4 = 0$, represented as 11000, and continue permuting it. Note that after “lift+1” steps, we return to the original vector. Let’s denote this matrix as H , which is:

$$H = \begin{pmatrix} 1 & 1 & 0 & 0 & 0 \\ 0 & 1 & 1 & 0 & 0 \\ 0 & 0 & 1 & 1 & 0 \\ 0 & 0 & 0 & 1 & 1 \\ 1 & 0 & 0 & 0 & 1 \end{pmatrix} \quad (\text{B2})$$

The matrix H defines a classical code with $n = \text{lift} = 5$ bits and $k = n - \text{rank}(H) = 0$ logical bits. When there are no logical bits, the code’s distance is denoted as ∞ , resulting in a $[5, 0, \infty]$ code. Since H is of full rank, there are 0 logical bits. An intuitive way to understand this is by considering that we initially have n physical degrees of freedom. The rank of H , which represents the number of stabilizers, imposes constraints. When these constraints equal the number of physical degrees of freedom (as with a full-rank H), there is no room left for encoding logical information, leading to 0 logical bits. To obtain a logical bit, we can relax some of the constraints by deleting rows from H . For instance, if we remove the last row from H we get the following parity check matrix,

$$\tilde{H} = \begin{pmatrix} 1 & 1 & 0 & 0 & 0 \\ 0 & 1 & 1 & 0 & 0 \\ 0 & 0 & 1 & 1 & 0 \\ 0 & 0 & 0 & 1 & 1 \end{pmatrix}. \quad (\text{B3})$$

The rank of \tilde{H} is 4, which gives 1 logical bit, resulting in $[[5, 1, 5]]$ code. Similarly, by varying the rank of the matrix H and the lift, we can generate codes with different numbers of physical and logical bits. Next, let’s take

the hypergraph product of the repetition code shown in Fig. 13 with itself. In terms of factor graphs, this hypergraph product corresponds to the process described in Fig. 14. The resulting quantum code is a $[[41, 1, 5]]$ surface code.

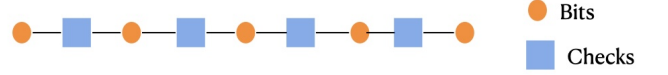


FIG. 13. Factor graph of the distance-5 repetition code: Orange circular nodes represent bits, and purple square nodes represent checks. The corresponding parity check matrix is given in Eq. 6

As previously mentioned, we have $n_1 n_2$ sector-1 qubits and $(n_1 - k_1)(n_2 - k_2)$ sector-2 qubits. Sector-1 qubits are formed by the product of two classical bits, while sector-2 qubits are formed by the product of two classical checks. The product of a classical bit with a check creates an X -stabilizer (red), and the product of a check with a bit creates a Z -stabilizer (green). For the surface code, there is 1 logical qubit, with both its logical- X and logical- Z observables fully supported on sector-1 qubits 14. This arises from the symmetry in the hypergraph product relative to the classical codes. If we had started with a symmetric parity check matrix, we would obtain a toric code with 2 logical qubits and 4 logical observables. In that case, 2 logical observables would be supported by sector-1 qubits, and the remaining 2 by sector-2 qubits. However, for the surface code, the initial parity check matrix as shown in Eq. B3 lacks this symmetry, leading to an unequal distribution of logical observables between sector-1 and sector-2 qubits [49].

Recall that we started with the generator polynomial $h(x) = 1 + x$. The influence of this generator polynomial is evident in the shape of the stabilizers. Note the polynomial labeling of qubits shown in Fig. 14. Each green

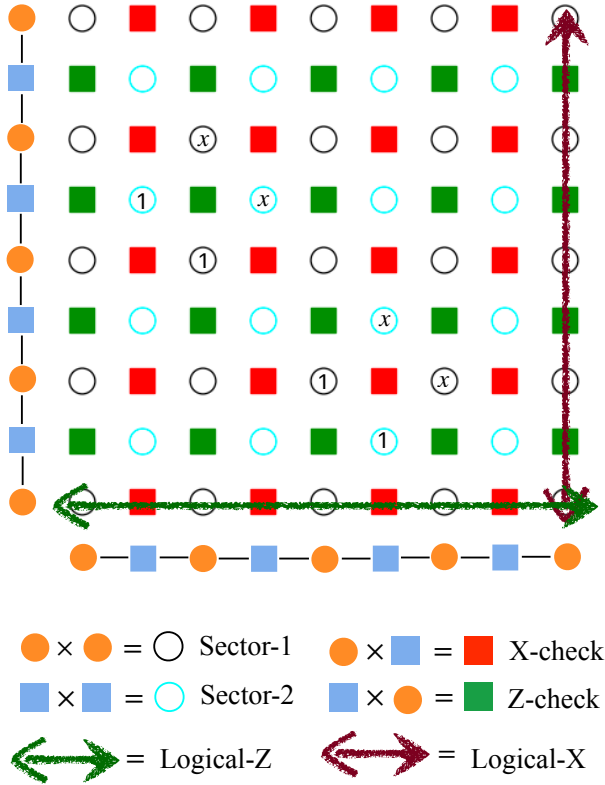


FIG. 14. A pictorial depiction of hypergraph product of distance = 5 repetition code with itself yielding a $d = 5$ surface code.

square represents a Z-stabilizer, while each red square represents an X-stabilizer. The support for each green or red square extends to its nearest neighbors on the left, right, top, and bottom.

2. Construction of HGP codes from

$$h(x) = 1 + x + x^3 + x^7$$

Let's consider the check matrix defined by $h(x) = 1 + x + x^3 + x^7$. We perform the hypergraph product of this check matrix with itself. Given that the degree of $h(x)$ is 7, the resulting quantum code with periodic boundary conditions will have a total of $2 \times 7^2 = 98$ logical qubits. Table IV lists the specifications of the code for different lifts.

We will use the codes in Table IV for our numerical studies. These codes were chosen because they provide 98 logical qubits with sufficient distance and require only a few thousand physical qubits. This makes them a promising option for near-term implementation.

Classical code corresponding to $h(x)$ with lift=15 gives us a $[15, 7, 5]$ code. Let us consider the first code from Table IV. This was obtained using hypergraph product of the parity check matrix H with itself. The classical code specified by H is: $C_1 = C_2 = [[15, 7, 5]]$, and by H^T

is $C_1^T = C_2^T = [[15, 7, 5]]$. The resulting quantum code is: $[[15^2 + 15^2 = 450, 7^2 + 7^2 = 98, 5]]$. As mentioned above, $15^2 = 225$ qubits belong to sector-1 and $15^2 = 225$ qubits belong to sector-2. The next step involves creating a $n_1 \times n_2$ lattice, which is $n_1 = n_2 = 15$ for our case thus, 15×15 two-dimensional lattice with each number corresponding to a qubit from sector-1. Then, place the qubits from sector-2 in between, as illustrated in Fig. 15.

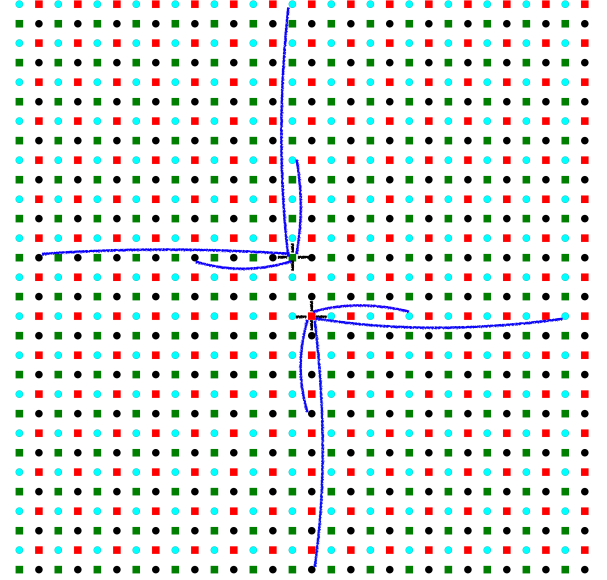


FIG. 15. 2-dimensional layout of $[[450, 98, 5]]$ code achieved via hypergraph product of check matrices $h(x) = 1 + x + x^3 + x^7$. Black circles indicate sector-1 qubits, while cyan circles denote sector-2 qubits. Additionally, red and green squares represent X and Z stabilizers, respectively. The layout displays one-to-one symmetry between sector-1 and sector-2 qubits.

We employ a mapping similar to the initial example to maintain manageability. We isolate the sector-1 and sector-2 qubits as before and observe symmetry between X and Z stabilizers. This characteristic is not unique to this particular code but is inherent in any hypergraph product code. Attempting to display all the stabilizers of codes listed in Table IV is impractical. Instead, we show the shape of a X and Z stabilizers in Fig. 15, and the remaining stabilizers can be derived by merely shifting the entire pattern horizontally and vertically with periodic boundary condition. Non-local gates for stabilizer measurements are shown in blue, while local gates are shown in black for both X and Z stabilizers.

In Fig. 15, black squares indicate sector-1 qubits, while cyan squares denote sector-2 qubits. Red and green rectangles represent X and Z stabilizers, respectively. We apply the same product method described in Fig. 14 to derive qubits and stabilizers from bits and checks, as in the surface code example above. Figure 15 depicts the shape of X and Z stabilizers. The red and green squares

represent the X-type and Z-type stabilizers, respectively. The influence of the check polynomial $h(x)$ on the shape of the stabilizers is evident. Additionally, we can see that the placement of sector-1 and sector-2 qubits is dual to each other, as are the shapes of the X and Z stabilizers, which is as expected. Understanding the shape and connectivity of stabilizers is crucial, as we will use cavities to do non-local gates. The stabilizer shape determines the optimal placement of these cavities.

With periodic boundary conditions, there is a one-to-one symmetry in the layout between sector-1 and sector-2 qubits, as well as between X and Z stabilizers, including the logical operators. Half of the logical operators are supported on sector-1 qubits, and the other half on sector-2 qubits. However, under open boundary conditions, gaps appear in the layout due to the asymmetric distribution of qubits between sectors, resulting from the unequal number of qubits in each sector. This disparity, caused by the open boundary condition, leads to all logical operators being fully supported on sector-1 qubits. We do not go into the details of the codes with open boundary conditions.

lift	Codes:Periodic Boundaries
15	[[450, 98, 5]]
30	[[1800, 98, 10]]
45	[[4050, 98, 15]]

TABLE IV. Quantum codes generated via hypergraph product of $h(x) = 1 + x + x^3 + x^7$ as the classical check matrix with itself with different lifts.

Appendix C: Decoding

The techniques for decoding quantum error-correcting codes are inspired by classical decoding algorithms. Notable examples include Belief Propagation [50], the Union-Find decoder [51], Minimum-Weight Perfect Matching [10], and Belief Propagation with Ordered Statistics Decoding [52], among others. The decoding problem can be formalized as follows:

$$He = s \quad (C1)$$

Here, H is the parity check matrix associated with the code, e is the error that occurred, and s is the syndrome obtained by measuring the stabilizers. Given s , the decoder determines the most likely correction operator c that produces the same syndrome s , $H \cdot c = s$, such that applying c together with e nullifies the syndrome, i.e.,

$$\begin{aligned} H \cdot (c + e) &= 0, \\ (e + c) &\in \text{rowspace}(H). \end{aligned} \quad (C2)$$

All algebraic operations are performed over the binary field $F_2^N = \{0, 1\}^N$ and are taken modulo 2. The condition $(e + c) \in \text{rowspace}(H)$ implies that the combined

operator $w = (e + c)$ must belong to the stabilizer group S . If $w \notin S$, a logical error has occurred, indicating that the decoding attempt has failed.

Our review of BPOSD decoder is guided by a comprehensive review paper by iOlius et al. [53] that provides an in-depth examination of various decoding algorithms. There are two key differences between decoding classical and quantum codes:

1. **Types of Errors:** Classical codes only address bit flip errors, while quantum codes must handle both bit flip and phase flip errors.
2. **Degeneracy:** In quantum codes, a single syndrome can correspond to multiple correction operators. This degeneracy means that several correction operators may satisfy the syndrome equation, but not all will correctly fix the error.

These differences make decoding quantum codes more complex than decoding classical codes. Let's define the two decoding problems:

- **Maximum likelihood decoding (MLD):** This method seeks to determine the most probable error pattern corresponding to the observed error syndrome. Specifically, it solves the following optimization problem:

$$\hat{E} = \operatorname{argmax}_{E \in \Pi^N} P(E|s) \quad (C3)$$

where P represents the probability distribution function of the error vector \hat{E} , Π^N denotes the N -qubit Pauli group, and s is the given syndrome. It is important to note that this method performs an exhaustive search over the Π^N group, disregarding the presence of degeneracy, and is thus referred to as non-degenerate decoding.

- **Degenerate Maximum likelihood decoding (DMLD):** An operator in the N -qubit Pauli group Π^N can be decomposed into three components: a pure error term forming the centralizer coset, a logical operator term forming the stabilizer coset, and a stabilizer component. An error operator E can be expressed in these three components to determine the exact stabilizer coset. Once the correct stabilizer coset is identified, any operator from this coset can be applied as a correction, as all elements in the stabilizer coset are equivalent up to a stabilizer, which acts trivially on the codespace.

The process of identifying the specific coset begins with a given syndrome, followed by the identification of the pure error component of the probable error operator, and finally, the logical component of the error. Mathematically, this is expressed as:

$$\hat{Q} = \operatorname{argmax}_{Q \in \mathcal{Q}} P(Q|s) \quad (C4)$$

where \mathcal{Q} represents the coset partitioning of the N -qubit Pauli group Π^N , and Q is the coset from this partition. \hat{Q} denotes the correct stabilizer coset, and once identified, any element of this coset can be used for correction, as they all have the same effect on the logical codewords. For a detailed description of coset partitioning, we refer to the work by Fuentes et al. [54].

As stated in [53], MLD problem has been proven to be NP-complete, while the Degenerate Maximum Likelihood Decoding (DMLD) problem falls into the #P complexity class. Problems in the #P class are computationally even more challenging than those in NP, presenting a significant obstacle to achieving the fast decoding necessary for effective quantum error correction [55]. According to [54], degeneracy should theoretically enhance the performance of quantum codes by allowing multiple errors to be corrected using the same recovery operation. In practice, degeneracy has indeed been shown to improve the performance of certain quantum codes. Moreover, decoders have been proposed that specifically address the challenges associated with degeneracy [56].

1. Belief Propagation (BP)

Belief Propagation (BP), also known as the Sum-Product Algorithm (SPA), is a message-passing algorithm used for inference on probabilistic graphical models. In this discussion, we will refer to this algorithm as BP. Given a syndrome s , BP aims to find the minimum-weight (MW) error pattern \hat{e} that satisfies $H\hat{e} = s$.

A classical or quantum error-correcting code can be succinctly represented using a Tanner graph or factor graph. For instance, Figs. 13 illustrate the factor graphs for a classical repetition code. In these graphs, derived from the parity-check matrix of a code, the columns correspond to bits/qubits, while the independent rows correspond to checks/stabilizer checks. A classical code includes a single type of check, which addresses only bit-flip errors. In contrast, a quantum code includes two types of checks: one for addressing X errors and another for addressing Z errors. Essentially, a quantum code can be seen as comprising two classical codes—one for protecting against X errors and another for Z errors.

The factor graph of a quantum code is a bipartite graph $G = (V \cup C, E)$, where V, C represent variable and check nodes, respectively, and E is the set of edges between nodes V and C . For example, Fig. 14 represents factor graph of surface code. We can see two types of checks, X (red) and Z (green) for correcting bit-flips and phase-flips. The edges correspond to the support of checks on physical qubits. Belief Propagation (BP) is employed as a message-passing algorithm between the nodes V and C .

For quantum codes, a modified version of BP, derived from its classical counterpart, is employed. In classical

codes, BP identifies the most likely error pattern given a syndrome, achieving a global optimum that resolves the syndrome equation. In contrast, for quantum codes, BP seeks the qubit-wise most likely error pattern, targeting a marginal optimum. This approach aims to identify an error configuration that maximizes the marginal probability of individual qubit flips. This can be mathematically represented as,

$$P_i(E_i) = \operatorname{argmax}_{\text{all configurations}} \sum P(E_1, \dots, E_i = 1, \dots, E_n | s). \quad (\text{C5})$$

The summation is performed over all possible configurations where $E_i = 1$ that satisfy the syndrome equation. Similarly, the bit-wise marginal probability is computed for each qubit. $P_i(E_i)$ represents the soft-decision for qubit i . The final decision is made using a hard-decision for each bit according to,

$$(E_{MW})_i = \begin{cases} 1 & \text{if } P_1(E_i) \geq 0.5 \\ 0 & \text{if } P_1(E_i) < 0.5 \end{cases}. \quad (\text{C6})$$

Here, $(E_{MW})_i$ represent the minimum weight configuration for qubit i among all possible configurations that satisfy Eq. C5. By determining the marginal for each qubit in this manner, we derive an overall minimum weight configuration that satisfies the given syndrome. The detailed description of each step of BP can be found in Appendix-C of [17]. BP is an effective decoding algorithm for classical codes with nearly loop-free factor graphs. Some classical codes have been shown to approach the Shannon limit capacity when decoded using BP [57, 58]. However, the factor graphs of quantum LDPC codes exhibit high degeneracy, as previously discussed. This increased degeneracy leads to factor graphs with numerous short loops, causing BP to become stuck and preventing it from converging to a solution—a phenomenon known as quantum trapping sets [59]. Consequently, BP encounters significant challenges when applied to quantum LDPC codes, failing to achieve a decoding threshold [17].

2. Post processing of BP: Ordered Statistics Decoding (OSD)

We previously discussed that BP struggles in the presence of short cycles in a factor/Tanner graph, failing to converge to a solution and resulting in the absence of a threshold and an error floor [60]. This issue becomes particularly evident at low physical error rates, where the hard decisions based on soft decisions start to introduce errors. To address this challenge, a post-processing technique known as Ordered Statistics Decoding (OSD) was introduced after BP, collectively referred to as BPOSD. This approach was first implemented to quantum LDPC codes by Pantelev and Kalachev [45]. BPOSD initially

runs BP and then uses its output as the input for the OSD post-processing step. This approach has demonstrated strong performance across a range of random quantum LDPC codes, as evidenced in this work [45]. Their method performs remarkably well for any random quantum LDPC codes.

When BP fails to converge to a solution, the Ordered Statistics Decoding (OSD) post-processing step is invoked. Despite BP's inability to converge, it provides marginal probabilities for each qubit as shown in Eq. C5 and an estimate of the error pattern \hat{E} . However, not all estimates of BP are necessarily incorrect. OSD utilizes the marginal information from BP to find a valid solution. OSD comes in various complexities known as OSD- w , where $w \in [0, \dots, H]$ and $H \in N$. OSD-0 when $w = 0$ is the least complex case which we use in our simulations. The steps of OSD-0 goes as follows:

1. Utilize the marginals from Eq. C5 or the soft-outputs from BP, and rank them from most likely to least likely to have been flipped. Store this list of bit indices as [BP].
2. Reorder the columns of the parity-check matrix H according to the ranking of bit indices [BP], and denote the reordered matrix as Ξ .
3. Select the row-rank(H) columns of the reordered matrix Ξ , denoted as $\Xi_{[BP]}$. Ensure that these selected columns are linearly independent, as the new matrix must have full rank.
4. Invert the matrix $\Xi_{[BP]}$ and solve the equation $\hat{E}_{[K]} = \Xi_{[BP]}^{-1} s$.
5. The final solution across all bits/qubits is given by $\hat{E} = [\hat{E}_{[K]}, \hat{E}_{[\bar{K}]}] = [\hat{E}_{[K]}, 0]$, where \bar{K} represents the most reliable set, which can be assumed to be zero. The OSD-0 will always satisfy the syndrome equation.

a. Higher order OSD

The motivation behind higher-order OSD is to find a solution \hat{E}_{Ξ_w} with a lower Hamming weight than the solution from OSD-0, denoted as \hat{E}_{Ξ_0} . OSD- w follows a process similar to OSD-0 up to the fourth step; the distinction lies in the fifth step. In OSD-0, the first four steps yield the vector $\hat{E}_{[K]}$. In OSD- w , we seek solutions $\hat{E}_{\Xi_w} = [\hat{E}_{[K]}, \hat{E}_{[\bar{K}]}]$, where $\hat{E}_{[\bar{K}]} \neq 0$ by solving:

$$\hat{\Xi}_{\Xi_w} = \left[\hat{E}_{[\bar{K}]}, \hat{E}_{[\bar{K}]} \right] = \left[\hat{E}_{[K]}^{w=0} + \Xi_{[K]}^{-1} \Xi_{[\bar{K}]} \hat{E}_{[\bar{K}]}, \hat{E}_{[\bar{K}]} \right], \quad (C7)$$

The vector $\hat{E}_{[\bar{K}]} \neq 0$ has a dimension of $n - \text{row-rank}(H)$, suggesting that, in theory, one could attempt to find a solution with minimal Hamming weight

by exploring all possible chains of lengths up to $n - \text{row-rank}(H)$. However, this approach is computationally intensive, making it practical only for short chain lengths. To mitigate this challenge, the authors of [17] proposed the combination sweep strategy, a greedy search method that simplifies the identification of $\hat{E}_{[\bar{K}]}$. For more details, see Appendix B of [17].

OSD- w extends the search for a minimum Hamming weight solution beyond OSD-0. As the order w increases, the likelihood of finding a solution with minimal Hamming weight improves. However, this advantage comes with the cost of higher computational complexity. For instance, we compared the performance of OSD- w and OSD-0 and found no significant difference. However, varying the parameter w (OSD-4,5,6,7) resulted in a considerable increase in computation time compared to OSD-0. Therefore, we opted to use OSD-0.

Appendix D: Simulating errors in STIM

We initiate the ancilla state, ρ , in the all-zero state and attempt to encode ρ into a GHZ state using the cavity. However, as mentioned in the main text, in the presence of losses, the effect of the cavity can be described by map:

$$\mathcal{E}_{D^{-1}}(\rho) = \tau + \frac{2\theta}{\sqrt{C}d_N} \hat{J}_x \tau \hat{J}_x, \quad (D1)$$

where τ is the perfect GHZ state. The cavity error introduces a bit-flip on any of the participating qubits with equal probability p given by $2\theta/\sqrt{C}d_N$. Due to the limitations of STIM, we cannot directly apply this map. To simulate the errors, we use the `CORRELATED_ERROR` and `ELSE_CORRELATED_ERROR` functions. These two functions always appear in pairs, with the correlated term always preceding the else correlated term. We modify the probability arguments within these functions so that they apply a bit-flip to all participating qubits with the same probability.

Consider the example of a case where six qubits participate in a cavity operation, say for weight-6 GHZ state preparation. The final state will resemble Eq. D1. With some probability p , we may have a one-bit-flipped state. To model this scenario, we use the `CORRELATED_ERROR` and `ELSE_CORRELATED_ERROR` functions. Please refer to the code snippet below:

```

1 for kk in np.arange(len(sx_list)):
2     if kk==0:
3         hgc_circuit.append_operation("
4             CORRELATED_ERROR", stim.target_x
5             (sx_list[kk]+2*n), p_encoding/(
6                 len(sx_list)-kk*p_encoding))
7     else:
8         hgc_circuit.append_operation("
9             ELSE_CORRELATED_ERROR", stim.
10            target_x(sx_list[kk]+2*n),

```

```
p_encoding/(len(sx_list)-kk*
p_encoding))
```

where `len(sx_list)` represents the weight of the X -type stabilizer, and `p_encoding` denotes the cavity error probability. The following example illustrates the function of this code. All ancilla qubits (indexed as 106, 112, 118, 140, 141, and 142) have an equal probability of experiencing an X error, but in any given sampling, only one qubit will actually incur the error.

```
1 E(0.000166667) X106
2 ELSE_CORRELATED_ERROR(0.000166694) X112
3 ELSE_CORRELATED_ERROR(0.000166722) X118
4 ELSE_CORRELATED_ERROR(0.00016675) X140
5 ELSE_CORRELATED_ERROR(0.000166778) X141
6 ELSE_CORRELATED_ERROR(0.000166806) X142
```

Appendix E: Detailed simulation results

1. Results for codes generated from $h(x) = 1 + x + x^2$

Here we present all the simulation results. Figure 16 shows the results for Hardware-agnostic error model. See Fig. 17 for the results for custom error model. In both cases the ratio p_{cavity}/p_2 is varied. The title of each sub-figures shows the ratio. We fit all the plots for a given ratio to the equation,

$$P_L(p) = A \left(\frac{p}{p_{th}} \right)^{ad^b}, \quad (\text{E1})$$

The threshold is calculated using this fit function and is presented in Table II

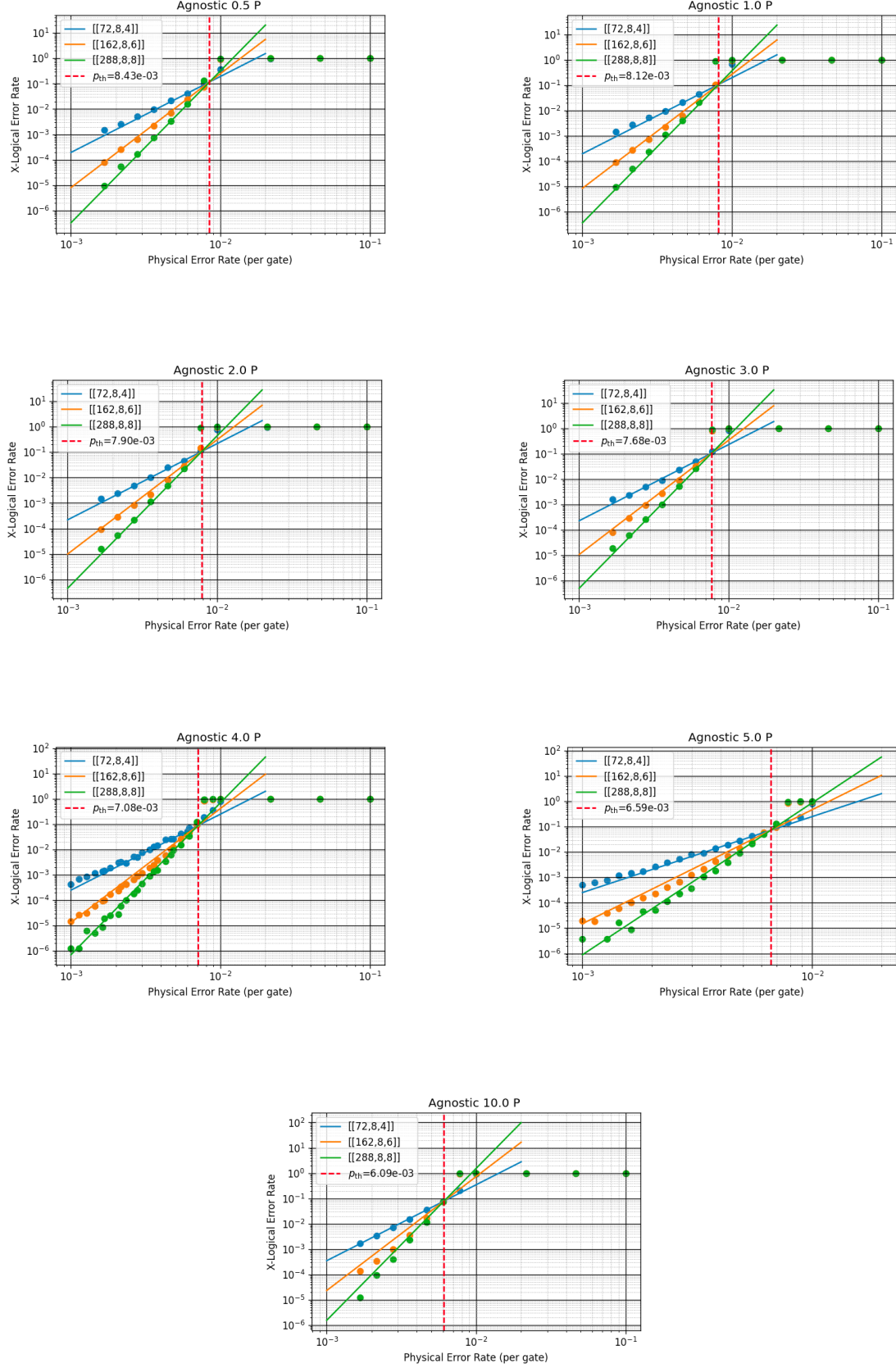


FIG. 16. Agnostic circuit-level noise simulation results for the codes listed in Table I. The plots are presented on a log-log scale, where the Y-axis represents the logical error rate and the X-axis represents the physical error rate (per gate). The simulations were carried out using STIM, with each data point based on 10^5 Monte Carlo samplings. The fitting lines were obtained using fitting Eq. 25.

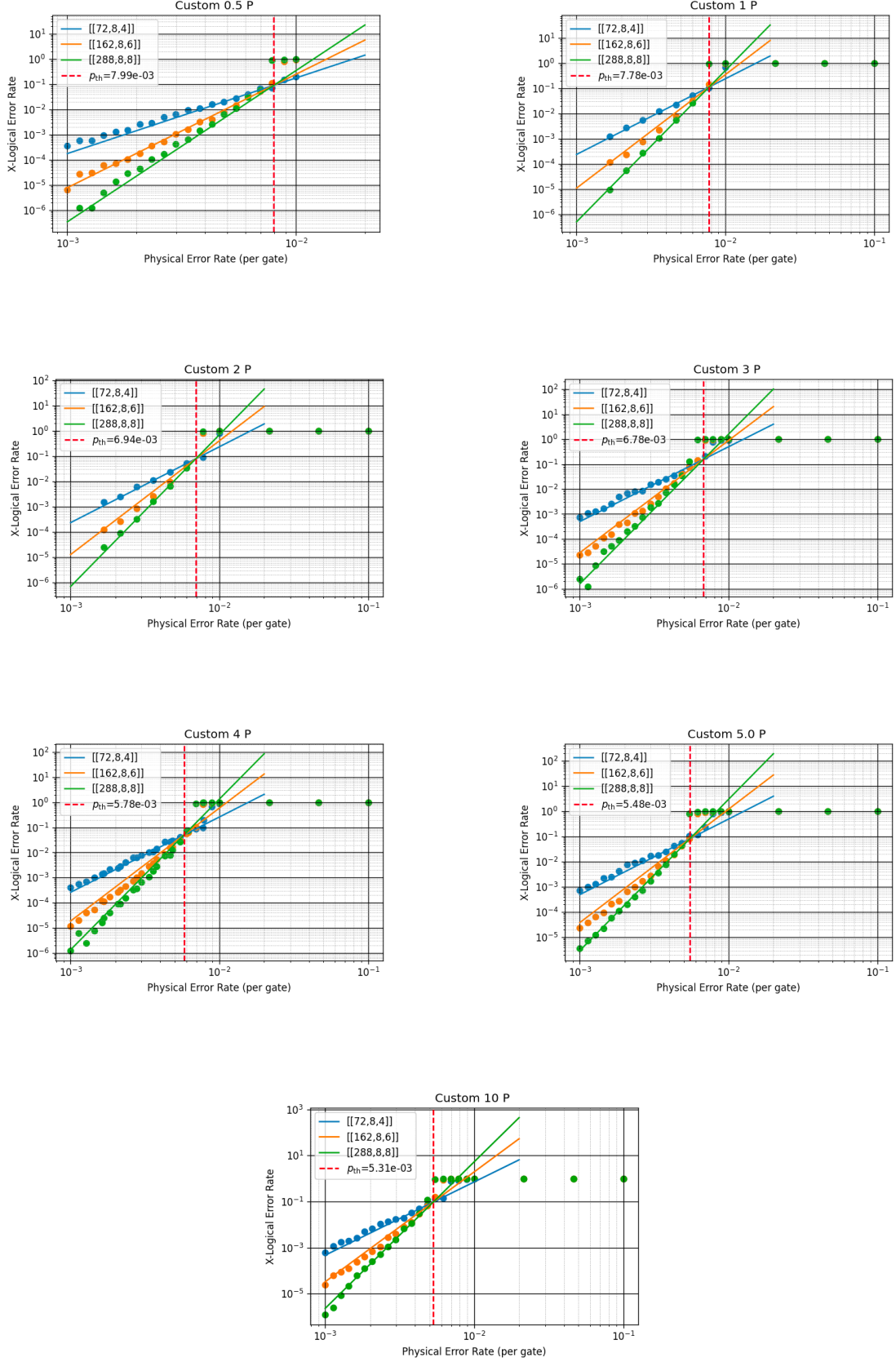


FIG. 17. Custom circuit-level noise simulation results for the codes listed in Table I. The plots are presented on a log-log scale, where the Y-axis represents the logical error rate and the X-axis represents the physical error rate (per gate). The simulations were carried out using STIM, with each data point based on 10^5 Monte Carlo samplings. The fitting lines were obtained using fitting Eq. 25.